Implementing the Blowers-Masel Approximation to Scale Activation Energy Based on Reaction Enthalpy in Mean-field Micro-kinetic Modeling for Catalytic Methane Partial Oxidation

Chao Xu,[†] Emily J. Mazeau,[†,‡] and Richard H. West[*,†]

†*Department of Chemical Engineering, Northeastern University, Boston, MA 02115, USA*

‡*Currently at: Oak Ridge National Laboratory, Oak Ridge, TN 37830, USA*

E-mail: r.west@northeastern.edu

Abstract

Mean-field micro-kinetic modeling is a powerful tool for catalyst design and the simulation of catalytic processes. The reaction enthalpies in a micro-kinetic model often need to be adjusted when changing species' binding energies to model different catalysts, when performing thermodynamic sensitivity analyses, and when fitting experimental data. When altering reaction enthalpies, the activation energies should also be reasonably altered, to ensure realistic reaction rates. The Blowers-Masel approximation (BMA) relates the reaction barrier to the reaction enthalpy. Unlike the Brønsted-Evans-Polani (BEP) relationship, the BMA requires less data because only one parameter, the intrinsic activation energy, needs to be determined. We validate this application of BMA relations to model surface reactions by comparing against density functional theory (DFT) data taken from literature. By incorporating the BMA rate description into the open-source Cantera software we enable a new workflow, demonstrated herein, allowing rapid screening of catalysts using linear scaling relationships

(LSRs) and BMA kinetics within the process simulation software. For demonstration purposes, a catalyst screening for catalytic methane partial oxidation (CMPO) on 81 hypothetical metals is conducted. We compare the results with and without BMA-corrected rates. The heat maps of various descriptors (e.g. CH_4 conversion, syngas yield) show that using BMA rates instead of Arrhenius rates (with constant activation energies) changes which metals are most active. Heat maps of sensitivity analyses can help identify which reactions or species are most influential in shaping the descriptor map patterns. Our findings indicate that while using BMA-adjusted rates didn't markedly affect the most sensitive reactions, it did change the most influential species.

Keywords

mean-field micro-kinetic modeling, Blowers-Masel approximation, sensitivity analyses, linear scaling, catalytic methane partial oxidation

1 Introduction

Heterogeneous catalysis plays a crucial role in the production of 80% of chemical products worldwide, and the catalyst market is expected to grow by 4.4% annually from 2020 to 2027.[1] Designing efficient and cost-effective catalysts necessitates an understanding of the underlying mechanism. This knowledge enables the optimization of catalyst morphology and reaction conditions, such as temperature and pressure, to improve catalyst performance. By manipulating the active sites and reaction conditions based on the reaction mechanism, catalysts can be designed to achieve higher levels of activity, selectivity, and stability. Mean-field micro-kinetic modeling (MKM) has proven to be a powerful tool to identify and interpret intermediates and reactions in processes such as gas-phase combustion[2,3] and catalysis,[4–6] and has been widely used for catalyst optimization. As demonstrated by its widespread and growing use,[7] MKM has the potential to help discover and design new catalysts to support

critical industrial processes.[8,9]

Furthermore, the linear scaling relationships (LSR) developed by Abild-Pedersen *et al.*[10] enhance the utility of MKM without excessive computational cost by creating a fast and simple way to predict the binding energy of surface species on different metal surfaces by using the adsorption energy of a species on one metal and scaling it to any other metal. While density functional theory (DFT) calculations are commonly used to compute the binding energies of surface species, performing DFT calculations for species on a large number of metals is computationally expensive. Consequently, LSRs are a useful approximation for rapidly estimating species' thermodynamic properties and screening potential catalysts.

It is important to note that adjusting species' enthalpies using linear scaling relationships can alter reaction enthalpies, necessitating the recalculation of transition states to ensure realistic reaction rates. As a substitute for DFT, and to reduce computational costs, the Brønsted-Evans-Polanyi (BEP) relationship,[11,12] a linear relationship between the reaction enthalpy and activation energy, is commonly employed in published works.[13–15] As discussed by Abild-Pedersen *et al.*,[10] a preliminary catalyst screening can be done by acquiring an estimate of the full energy diagram of surface reactions on a range of catalysts with linear scaling and BEP relations. This could be followed by DFT calculations or experiments on any promising catalyst found in the screening.

However, BEP parameters are not easy to derive due to the scarcity of thermodynamic and kinetic data for surface reactions. Furthermore, Blowers and Masel[16] pointed out that for certain reaction families, such as the hydrogen transfer reaction family, BEP relations behave poorly for extremely exothermic and endothermic reactions. They proposed an alternative approximation which is referred as the Blowers-Masel approximation (BMA) in this study. In addition to coupling with LSRs for catalyst screening, BMAs can be applied to adjust the reaction barrier in other situations where the reaction enthalpy needs to be modified, such as thermodynamic sensitivity analysis,[17,18] fitting thermodynamic data from experiments, and considering coverage effects in which the binding energy of an adsorbate changes with

its coverage.[19–21] Given their convenience and simplicity, BMAs could replace BEP relations for describing the activation energy as a function of reaction enthalpy.

In this work, BMAs were implemented in Cantera,[22] and demonstrated on a study of catalytic methane partial oxidation (CMPO).[23] Mazeau *et al.*[24] investigated the best catalyst for CMPO[25] by using LSRs to build micro-kinetic models on 81 hypothetical metals. In their work, the enthalpy of species on other metallic surfaces were scaled from a platinum surface using LSRs, but activation energies or reaction barriers were not changed. This work extends and builds on that study. To elucidate the use of BMAs in MKM, catalyst screening was conducted by applying LSRs to estimate species' enthalpies on 81 hypothetical metals for the CMPO model both with and without BMAs to see the effect of scaling the activation energy. A CMPO model over platinum was made with Reaction Mechanism Generator (RMG),[26,27] an open-source software for creating mean-field microkinetic models. A CMPO-BMA model was made by converting Arrhenius rate parameters in the CMPO model to BMA parameters while keeping the thermodynamic data fixed. The models with and without BMA parameters were then evaluated in a plug flow reactor (PFR) simulation with Cantera. Thermodynamic and kinetic sensitivity analyses were performed to compare the sensitivity of reactions and species before and after the Arrhenius parameters were converted to BMA parameters. LSRs were then used to scale the CMPO and CMPO-BMA models to 81 hypothetical metal surfaces from which heat maps were generated to compare the descriptor values, such as CH_4 conversion and full oxidation yield, and their first order sensitivities. The two sets of heat maps were then compared to discuss the impact of using BMAs. The screening method presented in this paper can serve as a starting point for further investigation, such as by performing DFT calculations on the identified metals.

2 Methods

2.1 The Blowers-Masel Expression

Blowers and Masel[16] have highlighted that the applicability of BEP relations becomes limited in cases of highly exothermic or endothermic reactions because it can lead to negative activation energies and poor estimates. They derive a new form of expression we term the Blowers Masel Approximation (BMA). The derivation follows from a few approximations, each of which they supported with detailed quantum chemistry calculations.[16,28,29] First, consider an abstraction reaction of the form

$$\mathrm{A} + \mathrm{BC} \longrightarrow \mathrm{AB} + \mathrm{C}. \tag{1}$$

Blowers and Masel proposed that the potential energy surface $V(R)$ for such a reaction can be described as

$$V(R) = V_{AB} + V_{BC} + V_I, \tag{2}$$

where V_{AB} and V_{BC} are the potentials of AB and BC, and V_I is an interaction potential. They describe V_{AB} and V_{BC} using Morse potentials, and find that V_I can be described by

$$V_I = V_0 \exp\left(-\alpha_1 r_{\mathrm{AC}}\right) \tag{3}$$

where V_0 and α_1 are fitted parameters, and r_{AC} is the distance between atoms A and C. With ABC colinear the potential in (2) is rewritten as

$$\begin{aligned} V(R) =& w_F(\{\exp\left[\alpha_F(r_{AB} - r_{AB,equ})\right] - 1\}^2 - 1) \\ &+ w_B(\{\exp\left[\alpha_B(r_{BC} - r_{BC,equ})\right] - 1\}^2 - 1) \\ &+ V_0 \exp \alpha_1(r_{AB} + r_{BC}) \end{aligned} \tag{4}$$

where w_B is the B-C bond breaking energy, w_F is the A-B bond forming energy, $r_{AB,equ}$ and $r_{BC,equ}$ are the equilibrium bond lengths, α_B and α_F are the force constants for the bonds. The saddle point is located by setting the derivatives of $V(R)$ with respect to r_{AB} and r_{BC} equal to zero. By presuming a form of Badger's rule where

$$\frac{\alpha_F}{\alpha_B} = \frac{r_{AB,equ}}{r_{BC,equ}} \tag{5}$$

and using w_0 to represent the average of the bond breaking energy and the bond forming energy,

$$w_0 = \frac{w_B + w_F}{2}, \tag{6}$$

the analytical expression of the Blowers–Masel approximation (BMA) can be simplified to

$$Ea = \begin{cases} 0 & \text{for } \Delta H_{rxn} < -4E_a^0 \\ \Delta H_{rxn} & \text{for } \Delta H_{rxn} > 4E_a^0 \\ \frac{\left(w_0 + \frac{\Delta H_{rxn}}{2}\right)(V_P - 2w_0 + \Delta H_{rxn})^2}{V_P^2 - 4w_0^2 + \Delta H_{rxn}^2} & \text{otherwise} \end{cases} \tag{7}$$

where

$$V_p = 2w_0 \frac{w_0 + E_a^0}{w_0 - E_a^0} \tag{8}$$

E_a^0 is the intrinsic activation energy and equals the activation energy when $\Delta H_{rxn} = 0$, and w_0 is, from the derivation which applies to hydrogen transfer reactions, the average of the bond dissociation energy of the bond being broken and the bond being formed. It was found that w_0 does not significantly change the fitting results for surface reactions.

Blowers and Masel[16] demonstrated their expression fit well the data of the 151 hydrogen transfer reactions tabulated by NIST.[30] Because the validation data were for gas-phase reactions, the expression has not previously been shown to be applicable to surface reactions. To address this, we here use a variety of heterogeneous surface reactions, mostly taking E_a

and ΔH data from Catalysis-Hub,[31] an open DFT database for surface reactions.

The weak influence of w_0 in BMA fitting is demonstrated in Figure 1 using the reaction $CH_4 + 2* \rightleftharpoons CH_3* + H*$ where the $*$ represents the surface site. The points show E_a and

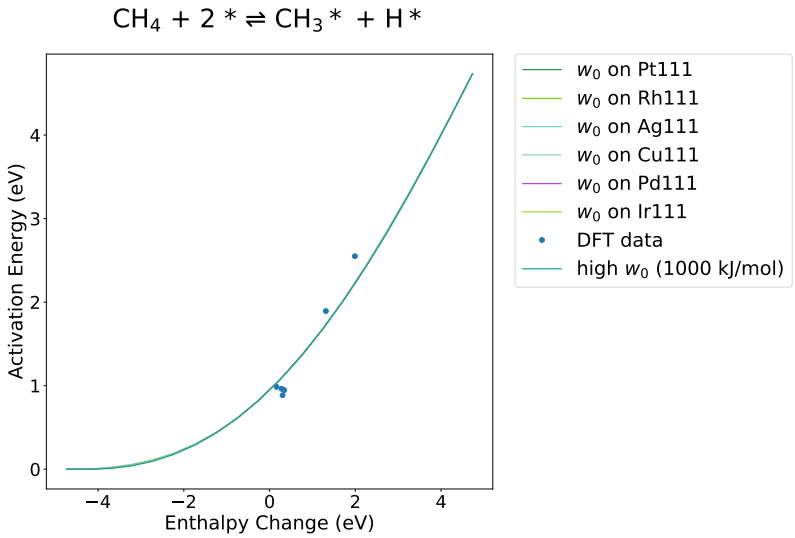

Figure 1: Comparison of BMA fitting with w_0 on 111 facet of different metals

ΔH values from Catalysis-Hub for different (111) metal surfaces. The lines show a best-fit BMA curve using w_0 values corresponding to each metal surface, as well as to a very high w_0 value of 1000 kJ/mol. The lines are coincident, showing that w_0 has little effect on the BMA fitting outcomes, as no prominent variation is observed. This holds as long as $w_0 > 2E_a^0$, so an arbitrary high value can be used. Due to the insensitivity of BMA fitting to the value of w_0 when it is high enough, we henceforth assign it a value of 1000 kJ/mol in the reaction rate calculation for convenience.

Given the minimal influence of w_0 on the activation energy, E_a^0 is the only parameter to be determined from the activation energy and enthalpy of a reaction. This dependence on a single parameter is a major benefit of the BMA approach. Therefore, any Arrhenius parameters of a reaction can be converted to BMA parameters with only the knowledge of the enthalpy of the reaction. BMA parameters allow the activation energy to be scaled accordingly if the reaction enthalpy is changed by LSR or other causes.

Following that, a comparison was performed between the BEP fittings and BMA fittings

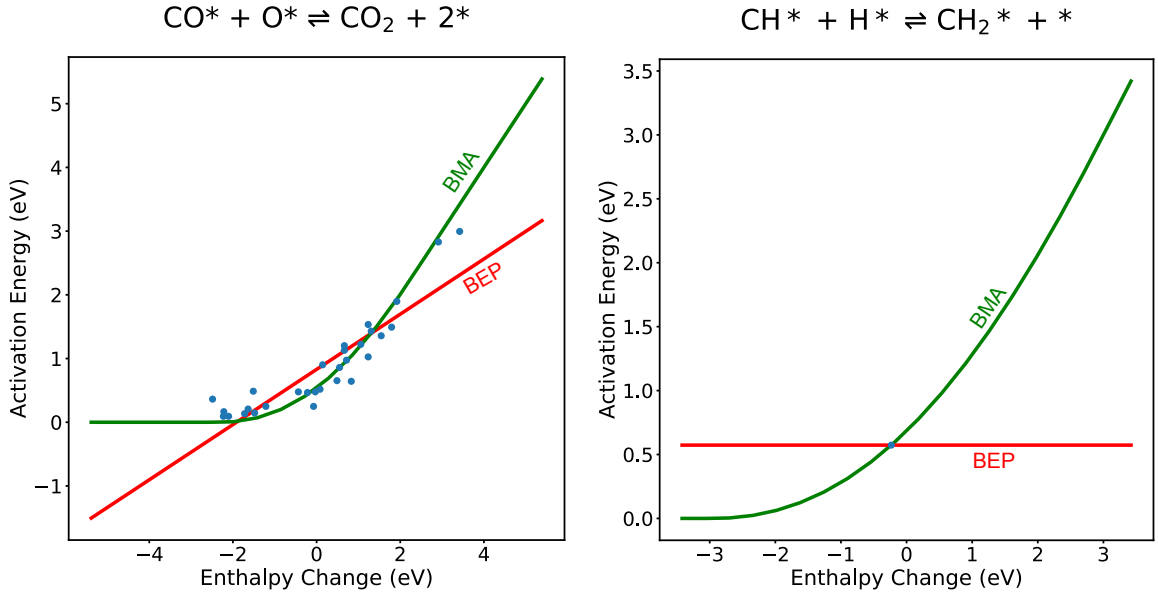

(a) (b)

Figure 2: (a) Comparison of BMA and BEP fitting with $w_0 = 1000$ kJ/mol;[32] (b) Comparison of BMA and BEP fitting with only one DFT data point;[33] BEP fitting is shown in red, BMA fitting is shown in green, and the DFT data are shown as blue dots

with $w_0 = 1000$ kJ/mol in the BMA fitting. Figure 2a compares the two fittings for carbon monoxide oxidation reaction $CO* + O* \rightleftharpoons CO_2 + 2*$ on metal oxide surfaces, with the DFT data generated and compiled by Kropp and Mavrikakis.[32] This reaction was chosen for demonstration because the available reaction enthalpy data covers a wide range from $-4E_a^0$ to $4E_a^0$. The root mean squared error (RMSE) of BMA is 0.22, while RMSE of BEP is 0.32. Note that the BEP fitting would predict negative activation energies at low ΔH values (< -1.9 eV), and barriers below the enthalpy of reaction for high ΔH >1.4 eV, whereas the BMA predictions do not have this problem. The BMA expression also fits the DFT data better than the BEP expression does in these extremes, and captures the curvature. Similar BEP and BMA comparisons were done for 14 reactions in the CMPO model which have DFT data on Catalysis-Hub, and the RMSEs all show a high degree of similarity, as included in supplementary materials Figure S1.

Figure 2b is the comparison between BMA and BEP when there is only one set of enthalpy and activation energy data available, for reaction $CH(s) + H(s) \rightleftharpoons CH_2(s)$. It is worth

noting that a BMA fitting can still be generated, whereas a BEP fitting is a flat line with an unknown slope (here assumed to be 0). This derivation of a BMA expression from a single reaction rate is how the Arrhenius rates are converted to BMA rates in Section 2.2.

The BMA is implemented in Cantera as a rate type which requires the pre-exponential factor A and accepts a temperature exponent b, like the modified Arrhenius equation in equation 9.

$$k = AT^b \exp \frac{-E_a}{RT} \tag{9}$$

Instead activation energy E_a in the Arrhenius rate, the BMA rate expression requires users to specify the intrinsic activation energy as `Ea0` and the average bond dissociation energy as `w`, as defined in equations (7) and (8), while the calculation of reaction enthalpy is handled internally by Cantera. An example of BMA rate expression input is

```
- equation: O2 + 2 X <=> 2 OX
  id: surface1-5
  rate-constant: {A:1.89e+11 m^5/mol^2/s, b:-0.5, Ea0:30 kJ/mol
     , w:1000 kJ/mol}
  type: Blowers-Masel
```

where the first line is the reaction equation, and the second line represents the reaction index. The fourth line designates the reaction type, which Cantera reads to select the appropriate built-in function for estimating the rate coefficient. It is important to highlight that the BMA rate constant is evaluated on the basis of the enthalpy at the temperature in the current system, rather than at 298 K. While Cantera generally works internally in SI units, input values can be provided using many different units. The units can be specified using a "units" mapping in the Cantera YAML input file[34] or written specifically for individual values like in this example. Modifications related to BMA were added to both C++ and Python code in Cantera, to enable the flexibility of using the code in multiple languages for reactor simulations.

2.2 Model Generation

Reaction Mechanism Generator (RMG)[26,27] is an open-source software to automatically build microkinetic models, with built-in thermodynamic and kinetic estimators and a database. RMG estimates the enthalpy of formation, entropy, and temperature-dependent heat capacity of a surface species by adding the properties of the gas-phase counterpart of the surface species and the difference caused by adsorption.[35] LSRs[10] are used to scale the binding energy of a surface species from Pt(111), to estimate adsorbate enthlapy on other metals. The adsorption estimates on Pt(111) are based on 69 species containing C/H/O/N. The data were calculated by Blondal *et al.*[36] using the Vienna ab initio simulation package (VASP)[37,38] with the BEEF-vdW functional[39] interfaced with Atomic Simulation Environment (ASE).[40] The gas-phase thermodynamic properties are calculated using Benson's group additivity and DFT.[26]

The reactions are determined by RMG kinetics families which describes the bond connectivity changes from reactants to products. Each reaction family has a hierarchical tree for rate estimations. Once the reaction family is chosen, the associated tree is searched to match the species, and the reaction with closest functional groups is used if there is not an exact match. The rate parameters in the trees are either acquired from a published model or estimated by averaging the parameters of similar reactions in the same family.[27] Besides the mentioned methods, published models are incorporated in RMG to provide thermo-kinetic parameter tables, which are referred to as libraries. The parameters are taken from the libraries if an exact reaction or species is found. RMG uses a rate-based algorithm[41] for model generation, which starts by reacting user-defined "core" species, with the product species being added to the "edge". During simulations at the user-specified conditions of interest, if the rate of production of an edge species is higher than the user-specified threshold, then it will be added to the core. The process is repeated until all edge species have a rate of

production lower than the threshold. The threshold is set by

$$R_{threshold} = \epsilon R_{characteristic} \tag{10}$$

where ϵ is a factor that can be assigned by user and the characteristic rate $R_{characteristic}$ can be written as

$$R_{characteristic} = \sqrt{\sum_{j \in core} R_j^2} \tag{11}$$

where R_j is the rate of production of species j in the core.

To make the CMPO model in RMG, the methane partial oxidation models developed by Quiceno *et al.*[42] and Mhadeshwar and Vlachos[43] were chosen as the reaction libraries for modeling the surface reaction network, and the model developed by Burke and coworkers[44] was used for gas-phase reactions. In order to provide the thermodynamics of the species, RMG relied on four libraries: **SurfaceThermoPt111**, **primaryThermoLibrary**, **thermo_DFT_CCSDTF12_BAC**, and **DFT_QCI_thermo**. These libraries contain thermodynamic data for gas and surface species obtained from ab initio calculations. **SurfaceThermoPt111** has the data for surface species on Pt, and the other three libraries have data for the gas-phase species. Species thermochemistry and reaction rates not found in these libraries are estimated by RMG. The model generation was started with 34 species, identified by Mazeau *et al.*,[24] in the core, as shown in the RMG input file in supplementary materials. Four surface batch reactors were added to verify the model for input ratios C/O= 0.6 and C/O= 2.6, both at 600 K and 2000 K. The absolute and relative tolerances for the ODE solver in RMG were 1×10^{-18} and 1×10^{-12}, respectively. The catalyst surface site density was set as 2.483×10^{-9} mol/cm^2,[24] and the remaining parameters can be found in the RMG input file in the supplementary material. Nine carbon binding energies evenly distributed from -5.5 eV to -7.5 eV and 9 oxygen binding energies from -3.25 eV to -5.25 eV were combined to define 81 hypothetical metal surfaces. A separate RMG model was constructed for each hypothetical metal surface, and these individual models were then

combined into a base model that includes all possible species and pathways that can occur significantly on any of the 81 hypothetical metals.

The thermodynamic data of species on other metal surfaces were modified from platinum by RMG using LSR during the model generation,[24] so the data were changed back to the original Pt(111) values when merging into the base model. Cantera was used to validate the base model. The BMA base model was made by converting all the Arrhenius parameters to BMA parameters using the enthalpy and activation energy of each reaction at 300 K and using the non-linear equation solver in the SciPy package[45] as described in section 2.1. The BMA fitting results for each reaction can be found in the BMA Cantera input file in supplementary materials. Two sets of models for 81 hypothetical metals were generated using LSRs to scale the species' enthalpy from the original base model and the BMA base model. The models scaled from the BMA base model have different kinetics from the other set because the BMA changes the reaction barrier.

2.3 Reactor Simulation

Cantera was used to simulate the reactive flow through a plug-flow reactor (PFR), which was represented as a chain of 7000 continuous stirred tank reactors (CSTRs), following the approach of Mazeau *et al.*[24] This is sufficient to resolve the fast reactions in some of the simulations. The simulation results on platinum were compared with experimental data.[25] The parameters of the reactor are shown in Table 1.

Table 1: PFR parameters[25] used for Cantera simulations

Inlet Gas Temperature	800 K
Reactor Length	7 cm
Reactor Diameter	1.65 cm
Catalyst Porosity	0.81
Catalyst Area Per Volume	160 cm^{-1}
Inlet Flow Velocity	36.63 cm/s
Catalyst Length	1 cm
Catalyst Start Position	1 cm

The composition of inlet gas includes methane, oxygen, and argon, where the C/O ratios range from 0.6 to 1.4 incremented by 0.1 and from 1.6 to 2.6 incremented by 0.2. The ratio of Ar to O_2 is 79 : 21 at each C/O input ratio. The exit temperature, exit conversions of CH_4 and O_2, and the exit selectivities of CO, CO_2, H_2, and H_2O at each C/O ratio were used as descriptor benchmarks to compare to experimental data.[25]

Methane conversion, synthesis gas yield, and full oxidation yield were used to measure model performance over all the metals. Synthesis gas consists of CO and H_2 and full oxidation refers to gas composed of CO_2 and H_2O. A value of 1 would be assigned to denote the complete synthesis gas yield or full oxidation of one gas species. However, both descriptors involve two gas products, so the values can be combined, allowing for a maximum possible value of 2.

2.4 Sensitivity Analyses

Kinetic and thermodynamic sensitivity analyses were performed on all models generated in this work to explore the influence of the BMA expression on sensitivities. To calculate kinetic sensitivity, the rate of each surface reaction was perturbed by 1%, one at a time, and the change of the descriptor of interest at fixed position on the catalyst region was normalized by the change of the reaction rate, as written in Equation 12

$$S_i = \frac{\left(\frac{X_{perturbed} - X_{original}}{X_{original}}\right)}{\left(\frac{k_{i,perturbed} - k_{i,original}}{k_{i,original}}\right)}, \tag{12}$$

where S_i is the kinetic sensitivity with respect to reaction i, $k_{i,original}$ is the rate coefficient of reaction i, $k_{i,perturbed}$ is the rate coefficient of reaction i after perturbation, $X_{original}$ represents the value of a descriptor (e.g.CH_4 conversion), and $X_{perturbed}$ represents the descriptor value after the rate of reaction i is perturbed. The thermodynamic sensitivity was calculated by increasing the enthalpy of one adsorbate by 0.05 eV at a time and comparing the descriptor difference at a position on the catalyst. It is important to note that the enthalpy change is

not modified proportionally (*e.g.* by 1%) because the definition of zero enthalpy is arbitrary. We perturb H_j rather than G_j because it is more straightforward in Cantera, but since $\Delta G^\circ = \Delta H^\circ - T\Delta S^\circ$, if we assume $\delta S = 0$ then $\delta G = \delta H$ anyway and our analysis is analogous to Campbell's degree of thermodynamic rate control analysis.[46]

The expression of thermodynamic sensitivity can be written as Equation 13

$$S_j = \frac{\left(\frac{X_{perturbed} - X_{original}}{X_{original}}\right)}{H_{j,perturbed} - H_{j,original}}, \tag{13}$$

where S_j is the thermodynamic sensitivity with respect to species j and $H_{j,original}$ and $H_{j,perturbed}$ are the enthalpies of adsorbate j before and after perturbation. The kinetic sensitivity is unitless, while the unit of thermodynamic sensitivity is eV^{-1}.

Adding the BMA expression is expected to improve the accuracy of thermodynamic sensitivity analysis because the influence of enthalpies on reaction rates can be properly treated. In the limit of a small perturbation, the thermodynamic sensitivity in Equation 13 can be written as:

$$S_j = \frac{1}{X}\frac{\partial X}{\partial H_j}, \tag{14}$$

where X is the descriptor value and H_j is the enthalpy of adsorbate j. Considering that X is calculated through a large set of ordinary differential equations or differential-algebraic equations, and the system includes the forward rate constants k and species enthalpies H as parameters, X in Equation 14 can be expressed as $X(k, H, \ldots)$. If $k(H)$ is also a function of H, then using the chain rule, the partial derivative of X with respect to H_j is:

$$\frac{\partial X}{\partial H_j} = \left.\frac{\partial X}{\partial H_j}\right|_{k \text{ constant}} + \frac{\partial X}{\partial k}\frac{\partial k}{\partial H_j} \tag{15}$$

Here $\frac{\partial X}{\partial k}$ is the partial derivative of X with respect to k holding everything else constant, $\frac{\partial k}{\partial H_j}$ is the derivative of k with respect to H_j, and $\left.\frac{\partial X}{\partial H}\right|_{k \text{ constant}}$ represents the partial derivative of X with respect to H_j when treating k as a constant (i.e., ignoring the dependence of k on

H_j).

The Arrhenius rate expression is not affected by species enthalpy, so the $\partial k/\partial H_j$ term of Equation 15 is zero when using the original model with Arrhenius rates. On the contrary, reaction enthalpy is considered in the BMA rate expression, and because reaction enthalpy is a function of species enthalpy, the $(\partial X/\partial k)(\partial k/\partial H_j)$ term in Equation 15 is included. Thus, models with BMA expressions will give more realistic thermodynamic sensitivity results than models with only Arrhenius expressions. It is worth noting that because all our models use reversible reactions, Cantera ensures thermodynamic consistency by deriving the equilibrium constant from ΔG_{rxn}, and so the *reverse* rate coefficients depend on reaction enthalpy ΔH_{rxn} in both CMPO and CMPO-BMA models.

Positive sensitivity values indicate that increasing the reaction rate constant or species enthalpy leads to an increase in descriptors, while negative sensitivity values represent a decrease in descriptor values. Reactions happen at an extremely small timescale, and species' concentrations reach a steady state near the start of the catalyst zone in these simulations, so the catalyst surface to volume ratio is decreased to 5% of the value in [25] when doing sensitivity analyses and descriptor screenings. As a consequence, the distance from the beginning of the reactor to reach steady state is extended. This extension ensures that the chemistry happening at the descriptor sample position remains comparable between models with and without BMAs.

Calculating sensitivities by a finite difference method requires comparing small changes between numbers. When the numbers themselves are small (*eg.* for hypothetical metals with a strong carbon binding energy that lead to almost no reaction), the comparisons become noisy, and must be solved with very tight tolerances. The same hypothetical metals often have binding energies that lead to very stiff systems of ODEs, causing numerical difficulties converging to tight tolerances. These issues do not plague the main results, but make sensitivity analysis a challenge in some areas of the discovery space. To address the convergence issue and numerical noise for kinetic and thermodynamic sensitivity results,

we averaged the results of multiple Cantera simulations with 6 varying error tolerances, using relative error tolerances (rtol) of 10^{-n} and absolute error tolerances (atol) of 10^{-2n} for $n = \{5, 6, 7, 8, 9, 10\}$, at each C/O input ratio in the set {0.6, 1.0, 1.1, 1.2, 1.6, 2.0, 2.6}. This leads to 6 simulations for each species or reaction sensitivity calculation; simulations which failed as well as those positioned within the upper and lower quartiles were omitted from consideration, and the remaining results were averaged for analysis. As a result, the total number of simulations completed for thermodynamic and kinetic sensitivity analyses on 81 metals was 432054.

3 Results and Discussion

3.1 BMA Expression Conversion

The reaction pathways of the CMPO model can be found in the work done by Mazeau *et al.*[24] The conversion of CH_4 and O_2, selectivity of synthesis gas (CO, H_2) and full oxidized products (CO_2, H_2O), and temperature at the exit with respect to C/O input ratio are plotted against experimental data[25] for the CMPO and CMPO-BMA models on Pt(111) in Figure 3. The model was initially built and validated on rhodium,[24] so there is a distinguishable disagreement with the experimental data on platinum. Given that the primary objective of this study is to explore the effect of BMA rates, the model is used as is. Despite the difference from the experimental data, the trend of descriptors for CMPO and CMPO-BMA base models are very close by comparing Figure 3a and Figure 3b, which verifies a successful conversion from Arrhenius rate to BMA rate.

As implemented in Cantera, the activation energy in the BMA expression is calculated from the reaction enthalpy evaluated at the current system temperature, not a reference temperature of 298 K. The species' enthalpies are calculated using NASA polynomials as a function of temperature. The activation energy in the BMA rate parameters is therefore slightly affected by the temperature, causing a small deviation from the Arrhenius rates.

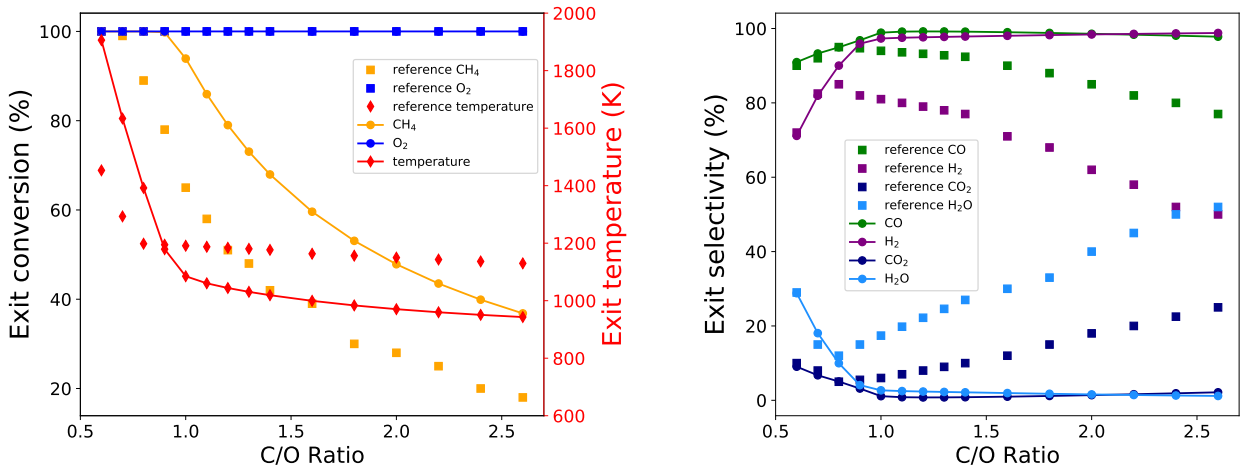

(a) CMPO model on Pt

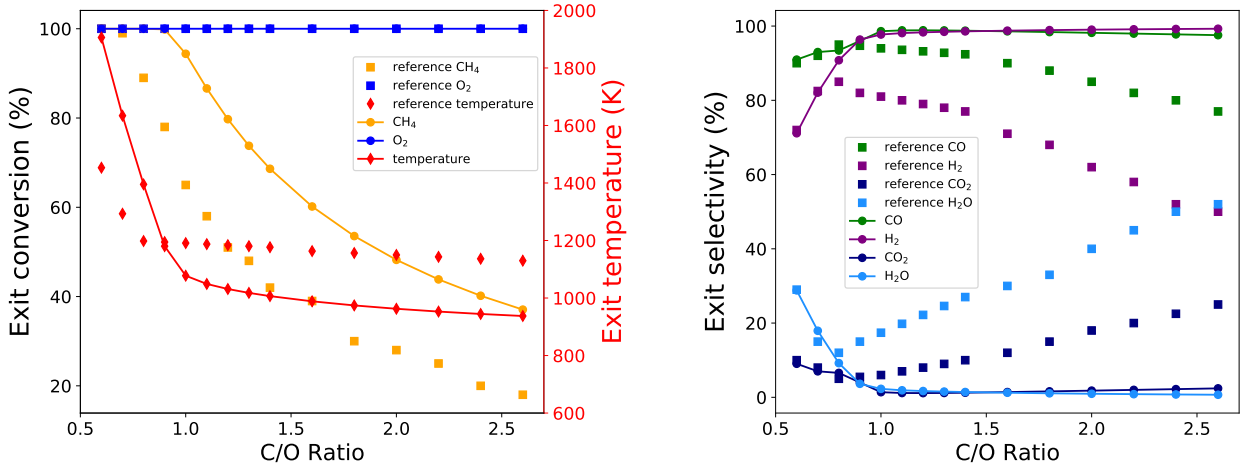

(b) CMPO-BMA model on Pt

Figure 3: Simulation comparison between CMPO and CMPO-BMA models on Pt, the two plots in 3a are the species conversion and selectivity change with respect to C/O input ratio for CMPO model on Pt, and the two plots in 3b are for CMPO-BMA model on Pt. The square dots represents the reference (experimental) data from previous research,[25] and the lines represents the simulation results.

Thus, minor differences between CMPO and CMPO-BMA models are observed in the synthesis gas conversion and full oxidation yield.

3.2 Sensitivity Analyses for CMPO and CMPO-BMA Models on Pt

3.2.1 Kinetic Sensitivity on Pt

As discussed in section 2.4, kinetic sensitivity should remain the same for CMPO and CMPO-BMA base models because only the pre-exponential parameter is modified by 1%. As illustrated in Figure 4, the sensitivity of CH_4 conversion at 1.045 cm (the 1045th CSTR in the simulation) to reactions with and without BMA rates are evaluated at C/O = 1.0, and the top 10 most sensitive reactions are plotted.

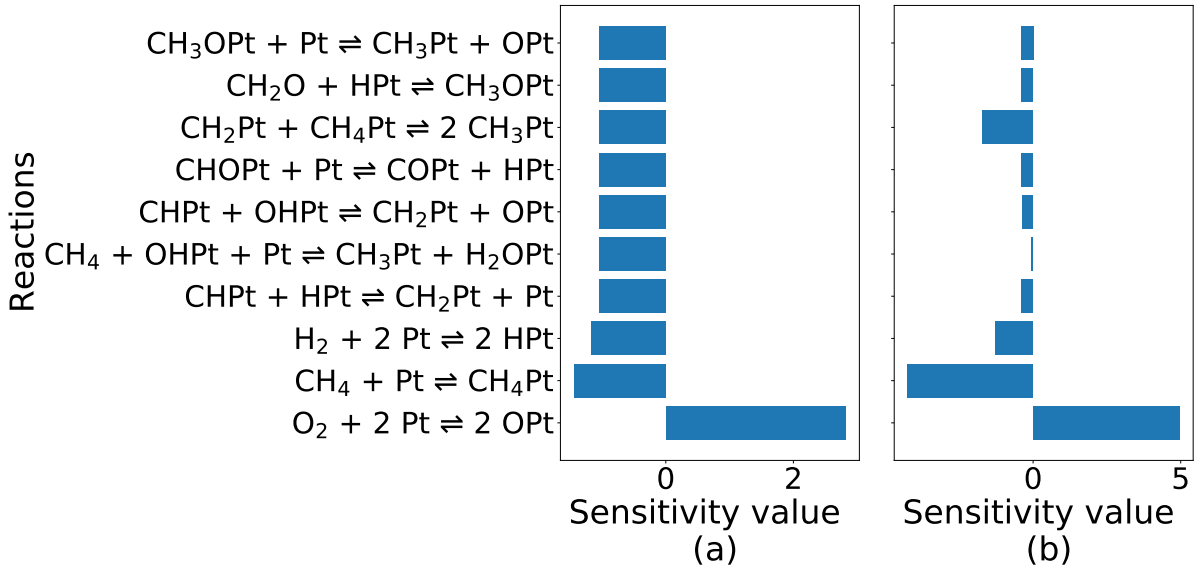

Figure 4: Kinetic sensitivity of CH_4 conversion to reactions for CMPO (a) and CMPO-BMA (b) models on Pt(111). The top 10 sensitive reactions are drawn at C/O= 1.0

$O_2 + 2\,Pt \rightleftharpoons 2\,OPt$ is the most positively sensitive reaction at C/O= 1.0 because the adsorbed oxygen further reacts with adsorbed carbon products to increase CH_4 conversion. The CH_4 physisorption reaction is the second most sensitive reaction, with a negatively

sensitivity for CH_4 conversion. Increasing the rate of CH_4 physisorption reduces the coverage of atomic oxygen and atomic hydrogen, so the subsequent reactions are slowed down. The sensitivity analysis of the subsequent reactions, as depicted in Figure 4, reveals a considerable degree of similarity among them within the CMPO base model, which means that the CH_4 conversion is equally sensitive to these reactions. In addition, the CMPO-BMA model has two reactions with high sensitivity, and the other eight reactions are much less sensitive. It is worth highlighting that both models agree on the top sensitive reactions, and the rank of most to least sensitive reactions does not change remarkably. The analogous ranks can be observed for the kinetic sensitivity of synthesis gas and full oxidation yield in Figure S2. There are several factors that could cause the disagreement between the two models. The temperature exerts a subtle influence on the BMA rates, resulting in a slightly deviated reaction rate change in the CMPO-BMA. This variance, albeit small, can have a marginal impact on the ongoing reaction pathway within each CSTR. Consequently, the chosen position for the kinetic sensitivity analysis (the 1045th reactor) does not exhibit precisely identical conditions for the two models. Another likely reason is the numerical error caused by the solver. The sensitivity (equation 12) is calculated as the ratio of two small numbers, the numerator being the small difference between two much larger numbers (in this case the conversion of CH_4 in the 1045th CSTR). This amplifies any small discrepancies due to numerical imprecision within the tolerances of the solver.

Raising the C/O input ratio to 2.6 leads to the same trends, as shown in supplementary material Figure S4. CH_4 conversion is not sensitive to most reactions except the dissociative adsorptions of O_2 and H_2. This is primarily due to the fact that CH_4 is the species with majority of coverage on the surface at the higher C/O input ratio, and changing the rates of these two reactions enhances the coverage of adsorbed atomic oxygen or hydrogen, thus promoting subsequent reactions. Increasing the rate of $O_2 + 2* \rightleftharpoons 2\,O*$ increases CH_4 conversion, and increasing the rate of $H_2 + 2* \rightleftharpoons 2\,H*$ decreases CH_4 conversion in both base models. It is worth emphasizing that the kinetic sensitivity analyses for the CMPO

and CMPO-BMA base models agree with each other for the most sensitive reactions, while showing differences in reactions that are relatively insensitive, and the sensitivity ranks of the two base models are more alike at higher C/O inlet ratio.

3.2.2 Thermodynamic Sensitivity on Pt

Meanwhile, thermodynamic sensitivity analysis (Figure 5) shows that the sensitivity of CH_4 conversion with respect to the enthalpy of each adsorbate is quite different between the models with and without BMA. Conversion is much more sensitive to changes in the enthalpy of CH_4* with the base BMA-CMPO model than with the base CMPO model at C/O= 1.0, and the most sensitive species is shifted from $CH*$ to $H*$ after the rate type is converted. In addition, increasing the enthalpy of adsorbed CO_2* decreases the conversion of CH_4 with Arrhenius rates, while it increases conversion with BMA rates. The similar sensitivity value shifts can be seen for the synthesis gas yield and full oxidation thermodynamic sensitivity analysis in Figure S3. The thermodynamic sensitivity analysis shows that the Arrhenius to BMA rate type modification can change the sensitivity of descriptors to species' enthalpies and could even lead to an opposite correlation between a descriptor and a species enthalpy. During the sensitivity analysis, the enthalpy of species was perturbed by 0.05 eV, subsequently impacting the enthalpy of reactions involving these species. Notably, in the CMPO-BMA model, the forward reaction barriers are enthalpy-dependent, while in the CMPO model they remain unaffected. Thus, this difference led to a discrepancy in the thermodynamic sensitivity analyses as shown in Equation 15.

3.3 Descriptor Screening Results

Simulations were repeated for the CMPO and CMPO-BMA models over all the 81 hypothetical metals, and the values of CH_4 conversion, synthesis gas yield, and full oxidation yield at 1.045 cm in the PFR, at C/O= 0.6, C/O= 1.0, and C/O=2.6 are demonstrated in heat maps in Figures 6, 7 and S5. The main point here is that when using the Blowers-Masel

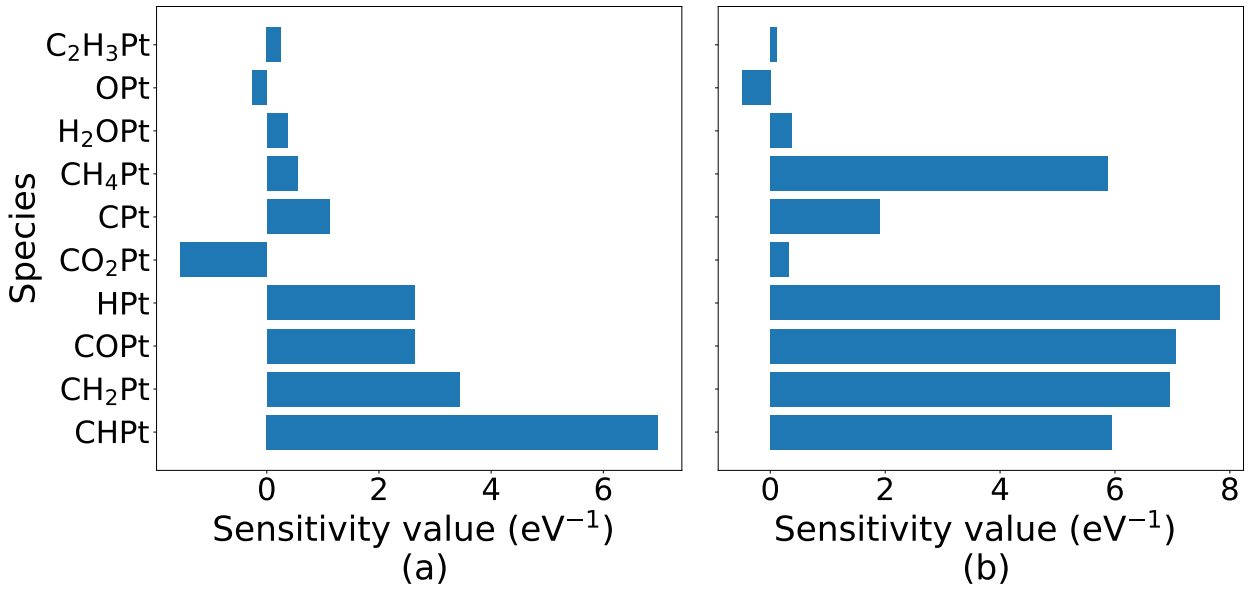

Figure 5: Thermodynamic sensitivity of CH_4 conversion to species for CMPO (a) and CMPO-BMA (b) models, the top 10 sensitive reactions are drawn at C/O= 1.0

approximation, the "hot spots" on the heat maps (the peaks of the volcano plots) move, and conclusions about what is the "best" candidate catalyst might change.

Comparing Figures 6a and 6d, the catalyst resulting in the highest CH_4 conversion at this point in the reactor move from near palladium and platinum, to a weaker carbon binding (ΔE^C is less negative) and weaker oxygen binding (ΔE^O is less negative). Comparing Figures 6b and 6e, the peak in yield of synthesis gas has moved to weaker oxygen binding (ΔE^O=-3.25 eV). Comparing Figures 6c and 6f, the peak in yield of full oxidation products (CO_2 and H_2O) has moved from ΔE^C=-6.75 eV, ΔE^O=-3.25 eV, towards stronger binding metals like Pt and Pd.

The values are plotted at 1.045 cm (the catalyst zone starts at 1.00 cm) to to highlight differences between simulations. For all cases, by the end of the PFR (7.0 cm) all simulations were either inert, or had similar high conversion and yield values, as shown in Figure S6 in the supplementary material.

To investigate the reason for the shift in peak CH_4 conversion from central to upper-right area, metals at the two different peaks ($\Delta E^C = -6.0$ eV, $\Delta E^O = -3.25$ eV and

$\Delta E^C = -7.25$ eV, $\Delta E^O = -4.25$ eV) were compared for both CMPO and CMPO-BMA models. The reaction path diagrams showing cumulative flux are shown in the supplementary material Figure S7 and S8.

For the CMPO-BMA model on the metal with ($\Delta E^C = -6.0$ eV, $\Delta E^O = -3.25$ eV) at C/O=0.6 (the hot spot in Figure 6d), the CH_4 conversion is higher because some is converted to C_2H_6 and C_2H_4 through gas phase reactions, pathways that are not active at that point in the CMPO model on the same metal (Figure S7). The gas phase rate constants were not changed, so this is likely because the temperature is higher in the BMA model due to faster exothermic reactions upstream in the adiabatic reactor simulation. This made the CMPO-BMA model consume 30% more CH_4 than the CMPO model on the same metal.

On the metal with ($\Delta E^C = -7.25$ eV, $\Delta E^O = -4.25$ eV) (the hot spot in Figure 6a), the main reaction pathways for the CMPO and CMPO-BMA models are similar as seen in supplementary material Figure S8, but the CMPO model has 12% higher amount of CH_4 reacted.

Overall, the CMPO-BMA screening plots at 1.045 cm from the beginning of PFRs have different shapes compared to CMPO plots. The principal cause is that BMA rates make the catalysis proceed faster in general, so the reaction pathways on certain metals differ from CMPO to CMPO-BMA models.

After increasing the input C/O ratio to 1.0, a similar story emerges (Figure 7). The peak of the volcano plot (the hot spot in the heat map) does not move significantly for CH_4 conversion or synthesis gas yield, but moves towards more weakly binding metals for the full oxidation yield (the bright zone moves up and right from Figure 7c to 7f). This is mostly due to the reaction $CO* + O* \rightleftharpoons CO_2 + 2*$ being faster in the CMPO-BMA models.

3.4 Energy Diagrams

To visualize the impact of BMA rates on reaction barriers, the energy diagrams of primary pathways on the metal characterized by $\Delta E^C = -6.0$ eV and $\Delta E^O = -3.25$ eV are com-

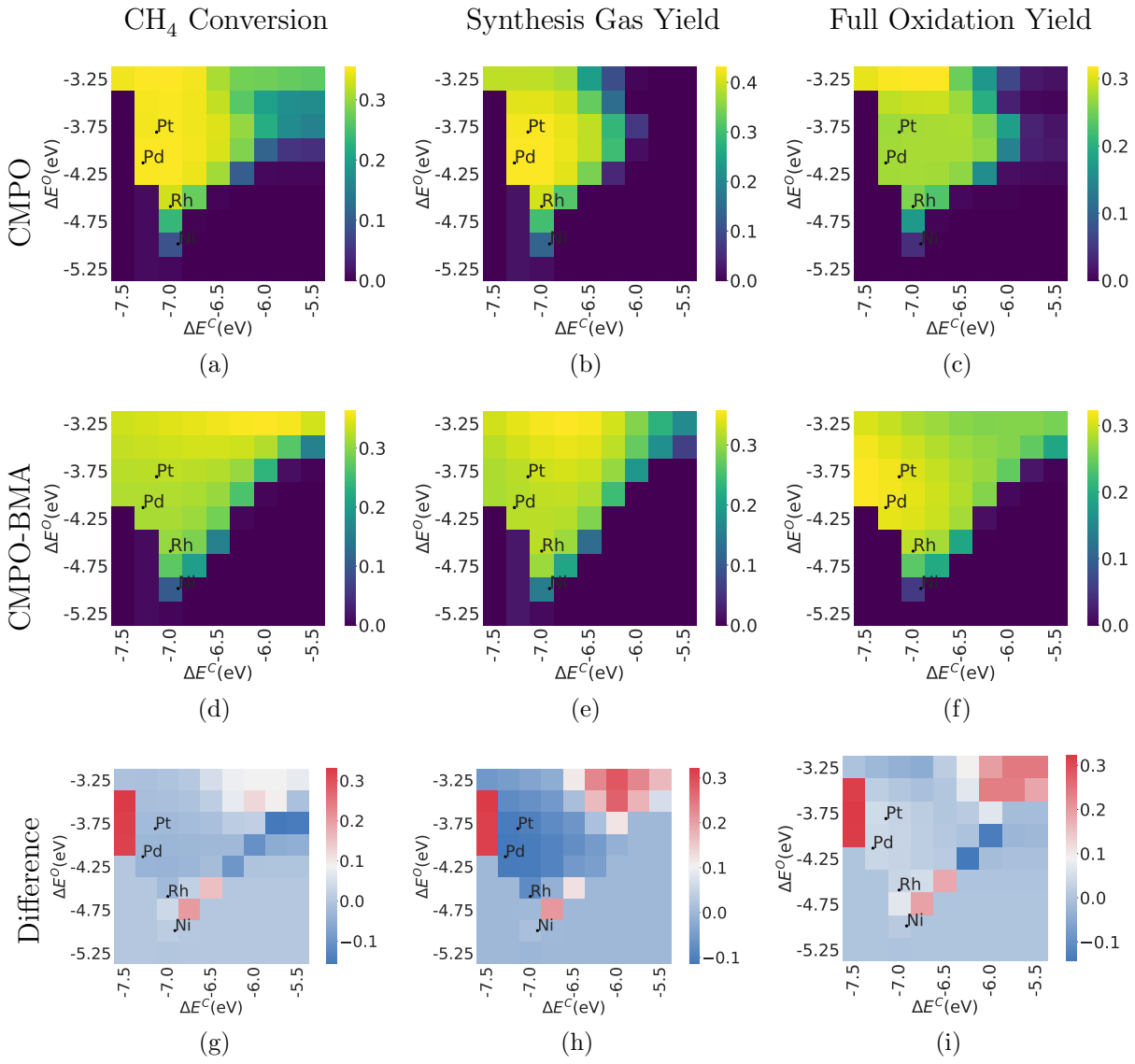

Figure 6: Comparison of CH_4, synthesis gas, and full oxidation conversion at C/O= 0.6 between CMPO (a, b, c) and CMPO-BMA (d, e, f) models. The third row is the difference between CMPO-BMA and CMPO models (g, h, i). The y-axis represents the binding energy of atomic oxygen, and the x-axis represents the binding energy of atomic carbon, each pixel represents a hypothetical metal interface.

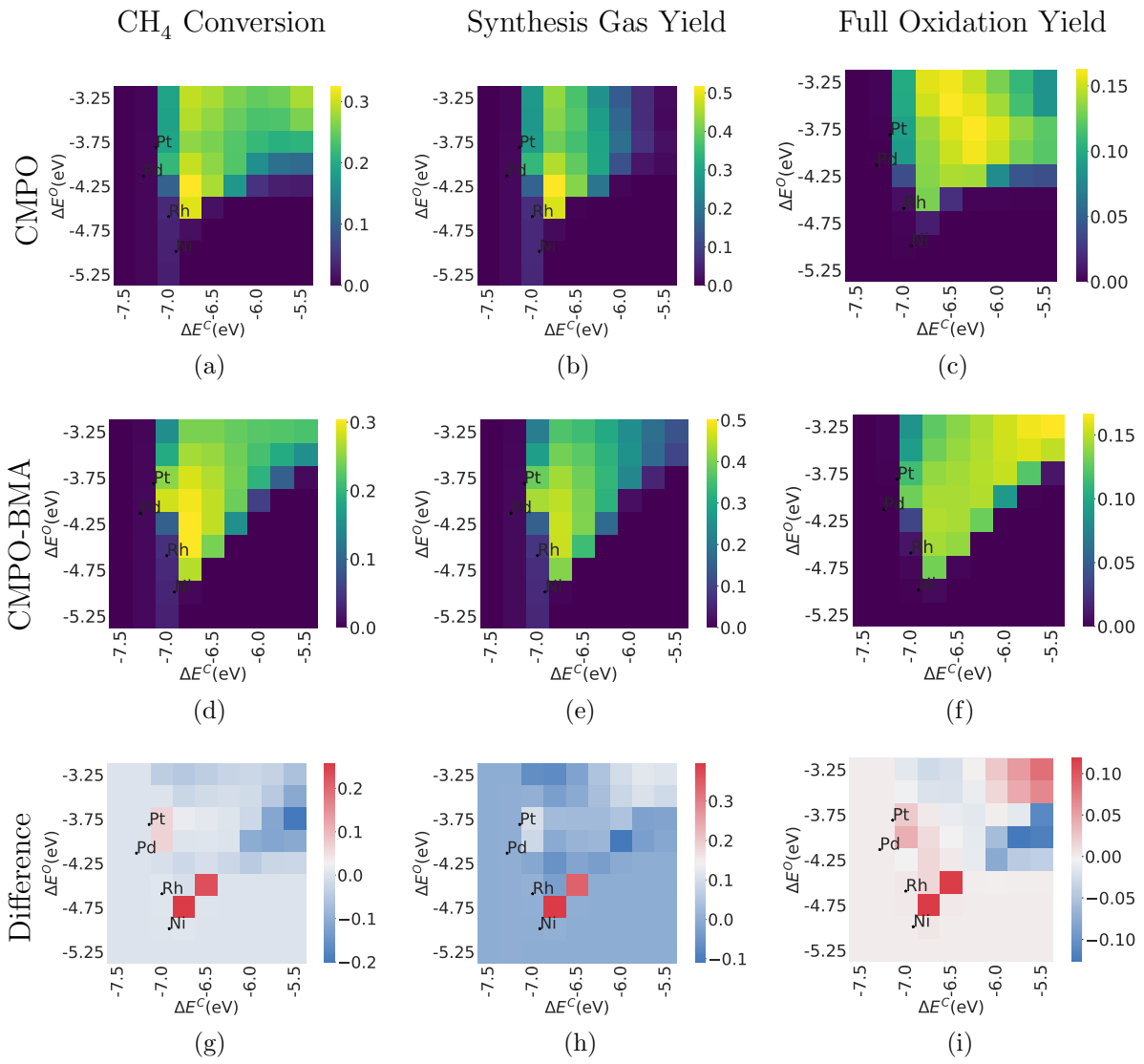

Figure 7: Comparison of CH_4, synthesis gas, and full oxidation conversion at C/O= 1.0 between CMPO (a, b, c) and CMPO-BMA (d, e, f) models. The third row is the difference between CMPO-BMA and CMPO models (g, h, i). The y-axis represents the binding energy of atomic oxygen and the x-axis represents the binding energy of atomic carbon. Each pixel represents a hypothetical metal interface.

pared for CMPO and CMPO-BMA models at C/O=0.6. This analysis aims to explain the heightened reactivity for that metal in CMPO-BMA models in Figure 6d, contrasting with the CMPO results in Figure 6a. The pathway flux diagrams on the metal can be found in supplementary material Figure S7. Figure 8 explores the dominant reaction pathway for

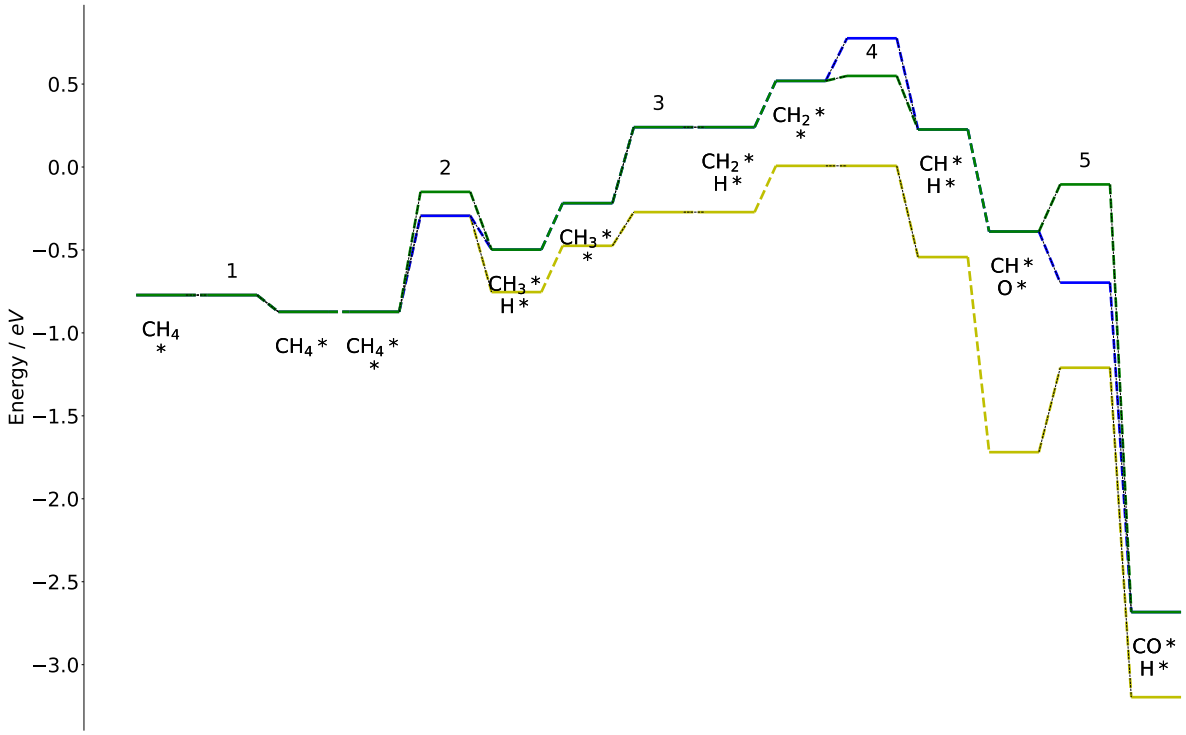

Figure 8: The energy diagrams for the main pathway on CMPO-BMA model on a hypothetical metal with $\Delta E^C = -6.0$ eV and $\Delta E^O = -3.25$ eV. The diagram comparison is drawn for CMPO model on Pt (yellow line), CMPO model (blue line), CMPO-BMA model(green line)

the CMPO-BMA model and the energy diagram for the identical pathway for the CMPO model. The reactions it goes through are listed in Table 2, the Arrhenius and BMA rate parameters for steps 3, 4, and 5 are written in the reversed direction in Cantera input files. Some reactions in the middle are omitted from Figure 8 for simplicity.

Gas-phase CH_4 initially adsorbed on the surface (step 1) before reacting with a vacant site $*$ to generate CH_3* and $H*$ (step 2). The third step happened through the reverse direction of reaction given in the model as $CH_2* + H* \rightleftharpoons CH_3* + *$. The barrier was kept still by the BMA even though LSR made the reaction (as written) slightly more exothermic, because the

Table 2: Dominant reactions to generate CO$*$ for the CMPO-BMA model on metal with $\Delta E^C = -6.0$ eV and $\Delta E^O = -3.25$ eV

Step #	Reaction
step 1	$CH_4 + * \rightleftharpoons CH_4*$
step 2	$CH_4* + * \rightleftharpoons CH_3* + H*$
step 3	$CH_3* + * \rightleftharpoons CH_2* + H*$
step 4	$CH_2* + * \rightleftharpoons CH* + H*$
step 5	$CH* + O* \rightleftharpoons CO* + H*$

reaction enthalpy was smaller than $-4E_a^0$. The reaction to achieve the fourth step was also written in the reversed direction in the model, as $CH*+H* \rightleftharpoons CH_2*+*$. This reaction was less endothermic on the hypothetical metal than on Pt, so BMA lowered its barrier (green line) based on the expression in range $-4E_a^0 < \Delta H_{rxn} < 4E_a^0$. In contrast, the CMPO model did not lower the barrier (in the reverse direction) of the Arrhenius expression, leading to a higher barrier (blue line) for step 4 and slower rate. Additionally, the activation energy in step 5 was estimated in the reverse, endothermic, direction (from adsorbed CO$*$ and H$*$ to CH$*$ and O$*$). LSRs altered it to be more endothermic on the hypothetical metal surface than on platinum. Thus the activation energy is raised by BMA according to the expression at range $\Delta H_{rxn} > 4E_a^0$. The CMPO model (blue line) does not raise the barrier for step 5, despite the reaction becoming more endothermic in the direction written, leading to an unreasonably low submerged barrier, but BMA is able to adjust the barrier to a reasonable level (green line).

Table 3 shows the main pathway for the CMPO model on the same hypothetical metal, and the energy diagram is plotted in Figure 9. Step 1 is the same as the main pathway

Table 3: Dominant reactions for the CMPO model on metal with $\Delta E^C = -6.0$ eV and $\Delta E^O = -3.25$ eV

Step #	Reaction
step 1	$CH_4 + * \rightleftharpoons CH_4*$
step 2	$CH_4* + O* \rightleftharpoons CH_3* + OH*$
step 3	$CH_3* + OH* \rightleftharpoons CH_3OH + 2*$

in the CMPO-BMA model in Table 2 and Figure 8. Then CH_4* reacted with O$*$ to form

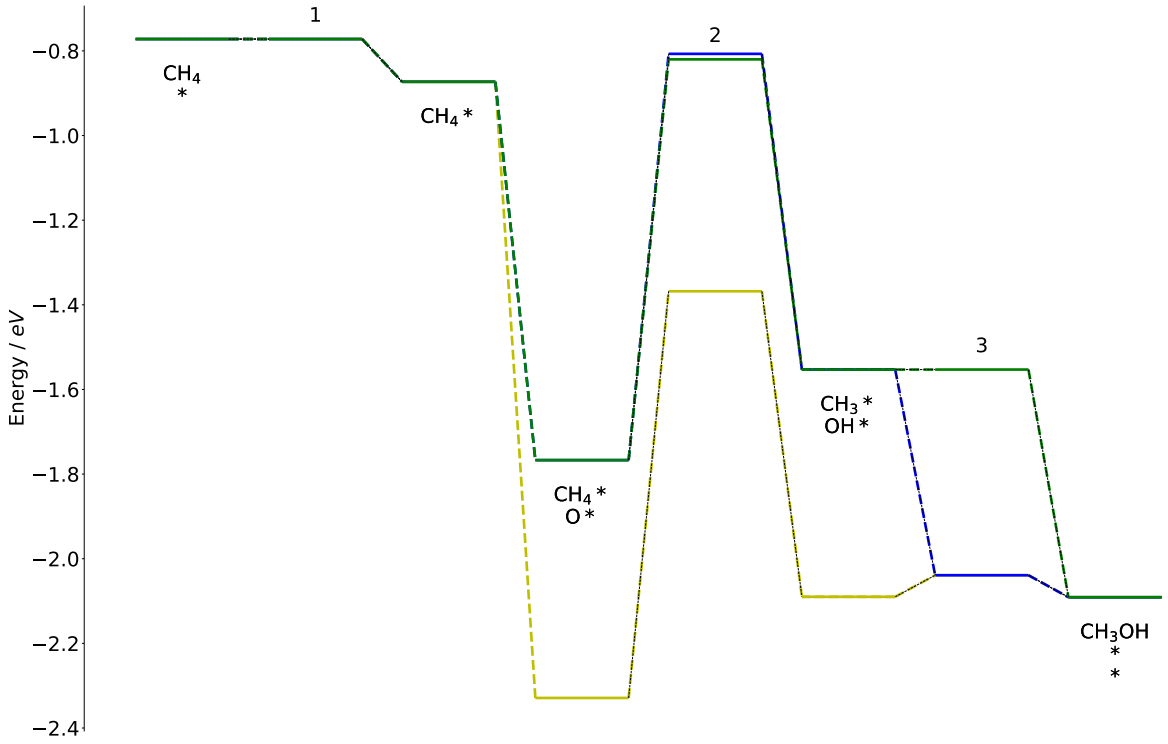

Figure 9: The energy diagrams for the main pathway on CMPO model on a hypothetical metal with $\Delta E^C = -6.0$ eV and $\Delta E^O = -3.25$ eV. The diagram comparison is drawn for CMPO model on Pt (yellow line), CMPO model (blue line), CMPO-BMA model(green line)

CH_3* and OH$*$ (step 2) with a similar barrier in both models. Step 3, which produces gas-phase CH_3OH, is presented as $CH_3OH + 2* \rightleftharpoons CH_3* + OH*$ with a low barrier on Pt(111) estimated by RMG (yellow). When scaling to the metal with $\Delta E^C = -6.0$ eV and $\Delta E^O = -3.25$ eV, the dissociative adsorption reaction becomes more endothermic, but the Arrhenius CMPO model does not raise the barrier (blue), leading to a too-fast net rate of progress from CH_3* to gas phase CH_3OH, and this reaction thus replaced the reaction from CH_3* to CH_2* as the primary reaction path. The CMPO-BMA model, however, raises the barrier (green) slowing the formation of gas phase CH_3OH, leaving more CH_3* on the surface to eventually form CO.

In conclusion, the unrealistic rate of progress of the reaction $CH_3* + OH* \longrightarrow CH_3OH + 2*$ was responsible for the low reactivity of the CMPO model on metal ($\Delta E^C = -6.0$ eV, $\Delta E^O = -3.25$ eV), and the BMA is able to raise the activation energy to prevent it. Consequently, a higher overall reactivity is seen on the same metal for the CMPO-BMA model.

3.5 Sensitivity Screening Results

Drawing upon previous investigations,[24] the technique of kinetic sensitivity screening has been established to identify the reactions that govern the abrupt drops in conversions observed in the heat map, i.e. the cliff edges of the volcano. In addition, we perform the analysis of thermodynamic sensitivity to identify the species accountable for the heat map pattern. It is anticipated that the BMAs will induce alterations in the results of thermodynamic sensitivity, as the intervention of BMAs, subsequent to species enthalpy modification through LSR, can potentially lead to shifts in reaction pathways. Therefore, the kinetic and thermodynamic sensitivity results for the CMPO and CMPO-BMA models are analyzed to explore the effect of BMA on the sensitivity screening results.

3.5.1 Kinetic Sensitivity

The kinetic sensitivity results on the base models identified that CH_4 conversion is most sensitive to the adsorption of CH_4 and O_2, so the kinetic sensitivity screening encompassing CH_4 conversion, synthesis gas, and full oxidation yield across the set of 81 metals was centered around these two reactions. As shown in Figure 10a, increasing the reaction rate of $CH_4 + * \rightleftharpoons CH_4*$ causes an increase of CH_4 conversion for both the CMPO and CMPO-BMA models on metals with carbon binding energy weaker than -6.75 eV. On the contrary, the metals on the left of the heatmap, in the column where $\Delta E^C = -7.0$ eV, demonstrate strong negative sensitivity in all the maps in Figure 10. The surface-to-carbon bond grows stronger from the right to the left of the heatmap, making it harder for carbonacious species to leave, leading to a higher coverage of carbonacious species. When the coverage is too high, the overall reactivity of the metal can be increased by slowing the adsorption reaction $CH_4 + * \rightleftharpoons CH_4*$) (negative sensitivity). When coverage is low, however, increasing the rate of adsorption increases the rate of reaction (positive sensitivity). Therefore, the pixels on the left of the heatmap have reversed sensitivity compared to the right side. The same trends can be observed for sythesis gas and full oxidation yields in Figure 10b and 10c.

The sensitivity heat maps of dissociative adsorption of oxygen shown in Figure 11 has a reversed trend compared to the physisorption of CH_4. The chemical process proceeds more rapidly due to 1% increase in oxygen adsorption rate on metals with strong carbon bonds ($\Delta E^C < -7$ eV) and weak oxygen bonds ($\Delta E^O > -4$ eV). This acceleration facilitates enhanced oxygen adsorption on the surface fostering the further reactions. The negative sensitivities appear only on the metals with strong oxygen bonds and low carbon bonds (bottom right corner) which have very low values in the descriptor screening maps in Figure 7, indicating that it is one of the reactions limiting the chemical process on these metals, because the coverage of oxygen is too high.

Because the BMA changes the activation energy of reactions based upon reaction enthalpy, the CMPO-BMA reaction rates differ from the CMPO rates on most metals, so the

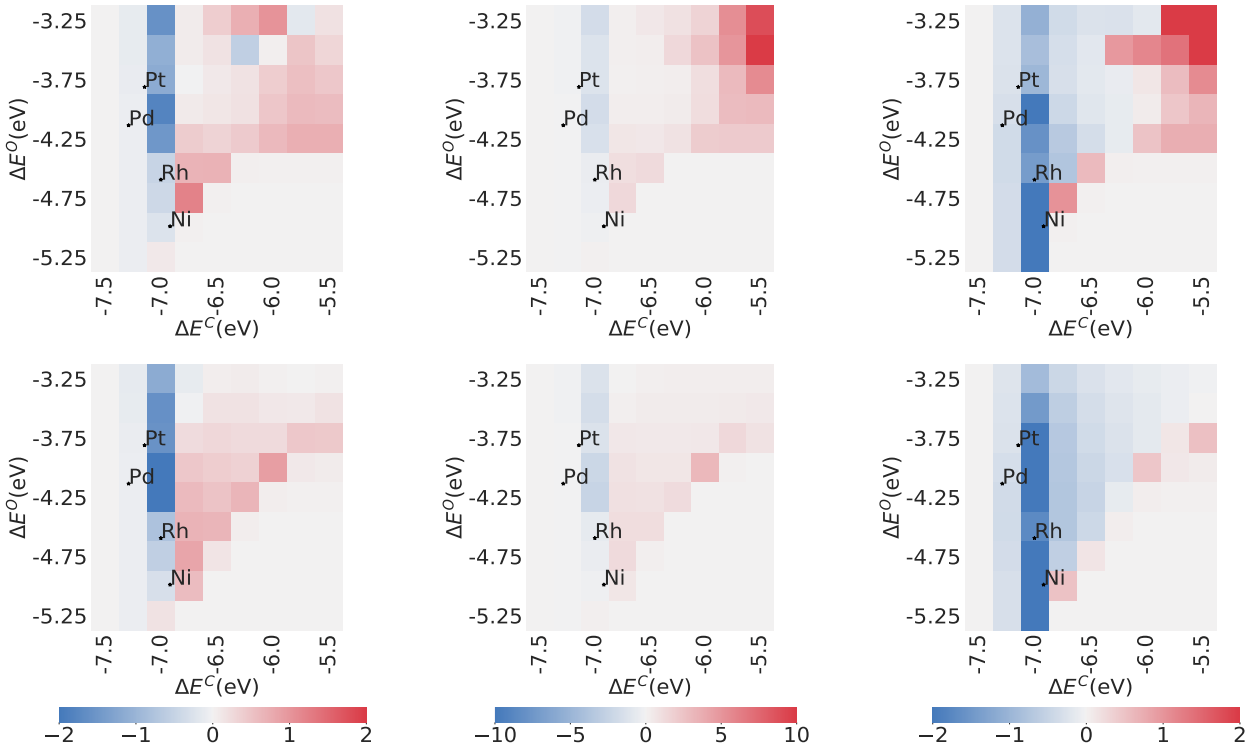

(a) CH_4 Conversion (b) Synthesis Gas Yield (c) Full Oxidation Yield

Figure 10: The kinetic sensitivity of CH_4 conversion (a), synthesis gas (b) and full oxidation yields (c) to the rate of methane physisorption reaction at C/O= 1.0, CMPO models are on the top, and CMPO-BMA models are at the bottom.

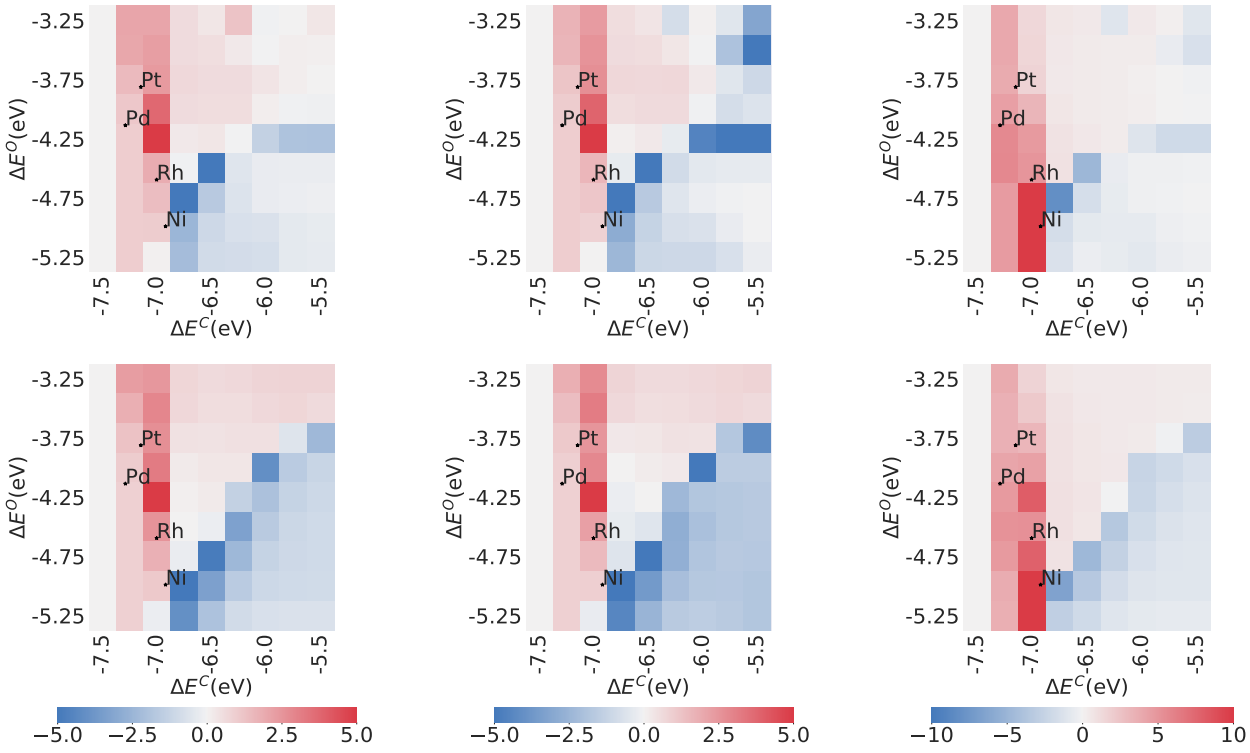

(a) CH_4 Conversion (b) Synthesis Gas Yield (c) Full Oxidation Yield

Figure 11: The kinetic sensitivity of CH_4 conversion (a), synthesis gas (b) and full oxidation yields (c) to the rate of oxygen dissociation adsorption reaction at C/O= 1.0, CMPO models are on the top, and CMPO-BMA models are at the bottom.

kinetic sensitivity screening results have slightly different values, but with similar trends. As discussed in section 3.4, the rate discrepancies also changed the dominant reaction pathways, which explains the different shapes of the descriptor maps between the two types of model.

The CH_4 physisorption reaction and O_2 dissociative adsorption are the most sensitive reactions, affecting most of the metal surfaces in the carbon and oxygen binding energy space explored, for both CMPO and CMPO-BMA models. Significant trends can be viewed across the metals, showing that these reactions are mostly responsible for the shapes of the descriptor heat maps. This suggests that incorporating BMA rates does not modify which reactions are the most sensitive reactions that dictate the shape of the descriptor heat maps.

3.5.2 Thermodynamic Sensitivity

In contrast to the kinetic sensitivity, the thermodynamic sensitivity heat maps in Figure 12 and Figure 13 show that species' thermodynamic sensitivity over the metals can change significantly after BMA rate substitution. Adsorbed water is negatively sensitive on about one fourth of the metals which have strong oxygen bonds and weak carbon bonds (bottom right) on the CMPO thermodynamic sensitivity heat maps of CH_4 conversion, synthesis gas, and full oxidation yields in Figure 12. It suggests that the enthalpy of adsorbed water is one of the factors limiting the descriptor values. However, the sensitivity values on CMPO-BMA screeing results in Figure 12 are more than 10 times smaller in general compared to CMPO models, indicating that the the enthalpy of adsorbed water does not contribute as substantially to the descriptor values.

The disparity is also evident in Figure 13, where the sensitivity of CH_4 conversion, synthesis gas, and full oxidation yield to the enthalpy of adsorbed hydroxide ($OH*$) exhibits pronounced negative values. While this effect is limited to metals in the lower right portion of the heat maps for CMPO models, a wider range of metals displays negative sensitivity values for CMPO-BMA models. It's noteworthy to highlight that for the CMPO-BMA models, on metals located in the active area (upper central portion) of the heat maps, the descriptors

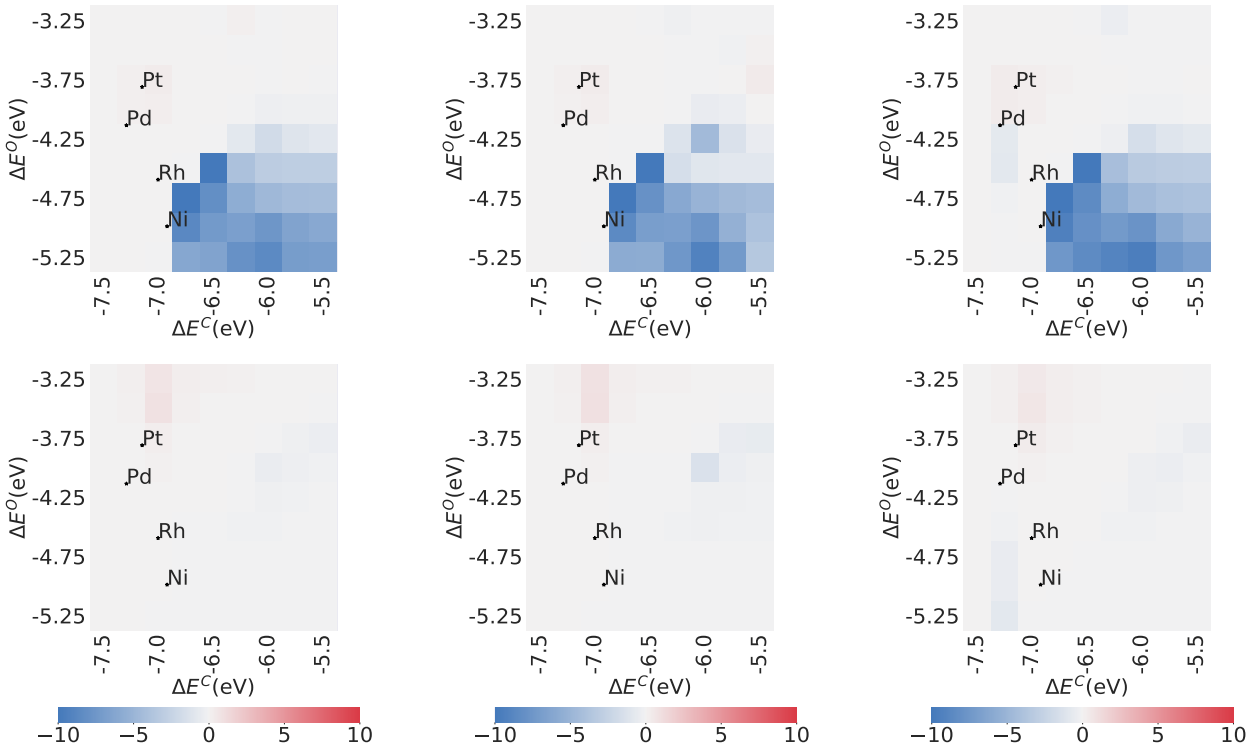

(a) CH_4 Conversion (b) Synthesis Gas Yield (c) Full Oxidation Yield

Figure 12: The thermodynamic sensitivity of CH_4 conversion (a), synthesis gas yield (b), and full oxidation yield (c) to the enthalpy of adsorbed water (H_2O*) at C/O= 1.0, CMPO models are on the top, and CMPO-BMA models are at the bottom.

exhibit positive sensitivity (mostly with sensitivity less than 1 eV^{-1}, except for the metal at $\Delta E^C = -7$ eV, $\Delta E^O = -4.25$ eV), with respect to the enthalpy of adsorbed hydroxide. However, in the corresponding area of the CMPO model heat maps, these sensitivity values are consistently zero.

Despite the outliers caused by the solver imprecision at the bottom right corner of the thermodynamic sensitivity screening for synthesis yield for CMPO-BMA models in Figure 13b, the screening results of thermodynamic sensitivity of adsorbed hydroxide show that using BMA rates make the species influential to methane oxidation on more metals compared to models with Arrhenius rates.

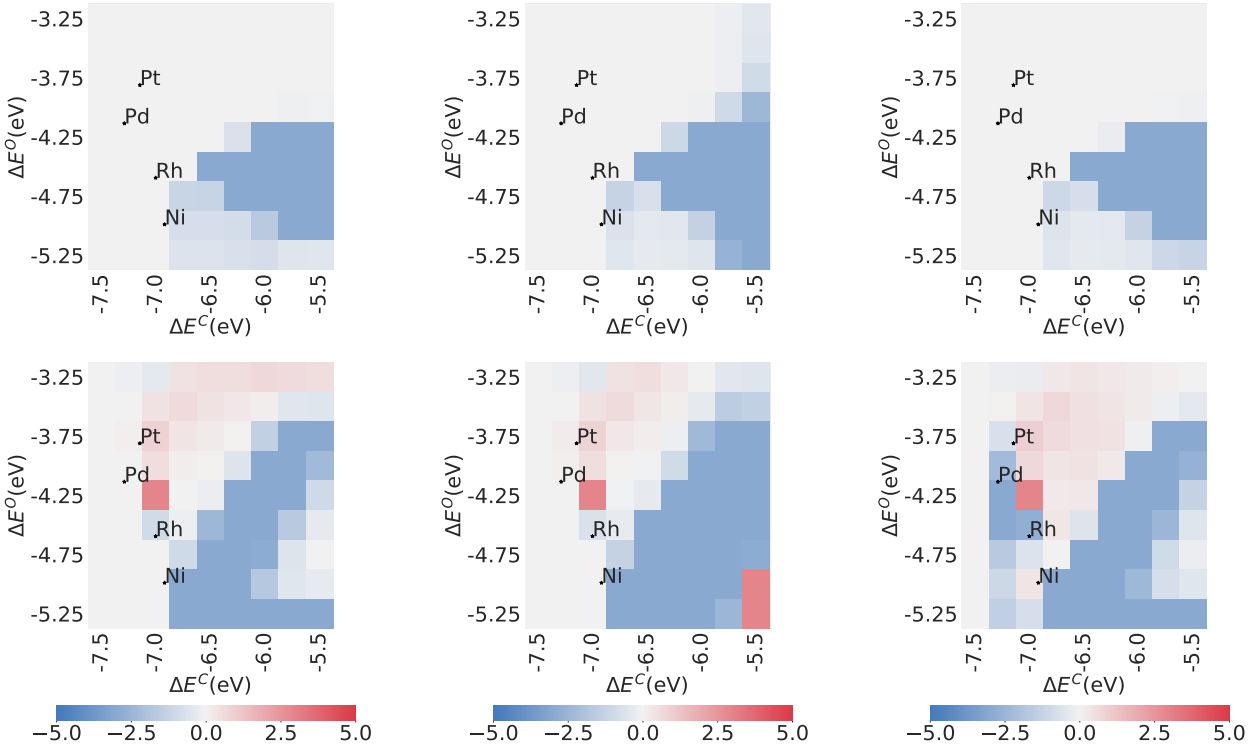

(a) CH_4 Conversion (b) Synthesis Gas Yield (c) Full Oxidation Yield

Figure 13: The thermodynamic sensitivity of CH_4 conversion (a), synthesis gas yield (b), and full oxidation yield (c) to the enthalpy of adsorbed hydroxide at C/O= 1.0, CMPO models are on the top, and CMPO-BMA models are at the bottom.

The thermodynamic sensitivity heat map analysis validates that BMA rates exert considerable impact on the thermodynamic sensitivities of some species engaged in the chemical

process. The introduction of BMA rates results in a shift in the dominant surface species governing the progression of methane oxidation across 81 metals. This influence stems from alterations in species enthalpy, which in turn affect the enthalpies and equilibrium constants of reactions involving those species. Consequently, the calculations of reverse reaction rates, relying on equilibrium constants and forward rate constants, are perturbed. Unlike Arrhenius rates, which remain unchanged, BMA rates adjust the forward rate constants, thereby impacting the overall rates of the associated reactions. This adjustment results in distinctive variations in CH_4 conversion, synthesis gas production, and full oxidation yields. In summary, applying BMA rates yields an alternative perspective on which species demand greater consideration during the optimization or catalyst design of the oxidation.

3.6 Conclusion

The BMA rate expression was successfully implemented in Cantera,[22] and CMPO models with and without BMA rates were compared. DFT data for 11 reactions in the CMPO base model were extracted from CatHub to validate the application of BMA to surface reactions. The CMPO base model on Pt was generated using RMG, and the BMA rates were fitted on the basis of Arrhenius rates to make a CMPO-BMA base model. A catalyst screening analysis on 81 hypothetical metal surfaces was carried out in Cantera using both CMPO and CMPO-BMA models to investigate the influence of BMA rates. The hypothetical metals were characterized using a combination of carbon binding energies of -7.5 eV to -5.5 eV and oxygen binding energies of -5.25 eV to -3.25 eV.

Simulations for the CMPO and CMPO-BMA base models on platinum were carried out in a PFR, which was approximated as a series of CSTRs in Cantera, with C/O input gas ratios from 0.6 to 2.6 to replicate the experimental work.[25] The models showed a noticeable difference compared against the experimental data, but general descriptor trends agreed. As the goal of this work was to explore the influence of BMA rates, we determined the RMG model has good enough agreement with experimental results and would be used as a base

model for comparison. The base model species concentration changes over the PFR were comparable, and the primary sensitive reactions for CH_4 conversion remained unchanged after converting from Arrhenius to BMA rates. The thermodynamic sensitivity analysis for the base models with and without BMA rates revealed that the BMA rates result in a significant change (up to 4 times) in the sensitivity of CH_4 conversion to species' enthalpies.

The screening results illustrate that when using the Blowers-Masel approximation, the "hot spots" on the heat maps (the peaks of the volcano plots) move, and the "best" candidate catalyst selected by the analysis can be altered. The metals that are most effective for synthesis gas yield for CMPO models have stronger oxygen bond (more negative binding energy) compared to the most effective metals for CMPO-BMA models at C/O=0.6. Furthermore, the metals that attain the highest CH_4 conversion and synthesis gas yield vary between the CMPO and CMPO-BMA models at low C/O input ratio, while at high C/O input ratios, active metals and the descriptor screening heat maps exhibit similar patterns. The difference in the descriptor screening results between CMPO and CMPO-BMA models primarily arises from certain expedited chemical processes due to the BMA rates.

The kinetic sensitivity heat map helps identify which reactions are most responsible for the shapes of the descriptor heat maps. The descriptors are most sensitive to the CH_4 adsorption and O_2 dissociative adsorption reactions, with and without BMA rates. This leads to the conclusion that BMA rates do not affect the most sensitive reactions identified using kinetic sensitivity analysis. However, the thermodynamic sensitivity heat maps showed that adsorbed water is a rate-determining species for many CMPO models, while it is not for CMPO-BMA models over the metals screened. The thermodynamic sensitivity heat maps of adsorbed hydroxide ($OH*$), however, showed the opposite. This observation suggests that the use of BMA rates can alter the conclusions drawn from a thermodynamic sensitivity analysis.

This work added a new feature to the open-source simulation software Cantera, allowing reaction kinetics to be specified using the Blowers-Masel approximation (BMA), in which the

reaction barriers are a function of the reaction enthalpy. Unlike the Brønsted-Evans-Polanyi (BEP) expression, this BMA form only requires one parameter (so it can be derived from a single reaction rate expression), and gives reasonable values when extrapolated to very high and low reaction enthalpies. We have shown that using BMA instead of simple Arrhenius expressions (with a fixed forward reaction barrier) during model analysis can lead to different results – both in the binding energies of the optimal catalyst, and in the relative importance of specific adsorbate enthalpies. Incorporating the BMA rate description into Cantera enables a new workflow, demonstrated herein, allowing rapid screening of catalysts using linear scaling relationships (LSRs) and BMA kinetics within the simulation software, with a single model input file. This can provide a starting point for a model of interest for further improvements. The workflow is not limited by the use of LSRs, since the BMA kinetics could equally well be combined with modern machine-learned predictors of adsorbate energies. This could be an efficient first step in a catalyst screening investigation, before further investigation (e.g. with DFT and then experiments) of any identified candidate catalysts.

Supporting Information Available

The Supporting Information is available free of charge at https://doi.org/(to be determined by publisher). Blowers-Masel approximation fittings for the DFT data extracted from Catalysis-Hub; kinetic and thermodynamic sensitivity of sythesis gas yield and full oxidation for the CMPO and CMPO-BMA base Pt(111) models at C/O=1.0; kinetic sensitivity of CH_4 conversion, synthesis gas yield, and full oxidation for CMPO and CMPO-BMA base models at C/O=2.6; descriptor screening results for CMPO and CMPO-BMA models at C/O=2.6; descriptor screening results at the end of PFR for CMPO and CMPO-BMA models at C/O=0.6; the reaction pathway for the CMPO and the CMPO-BMA model on the metal at ($\Delta E^O = -3.25$ eV, $\Delta E^C = -6.0$ eV); the reaction pathway for the CMPO and the CMPO-BMA model on the metal at ($\Delta E^O = -4.25$ eV, $\Delta E^C = -7.25$ eV)(PDF); RMG

input file for the base model, microkinetic model for Pt(111) in Cantera format, microkinetic models on all the hypothetical metal surfaces with and without BMA rates, Python scripts and Jupyter notebooks for running the simulations and sensitivity analyses, fitting Blowers-Masel rates, and reproducing the plots in the paper. (ZIP) More scripts can be found on the Github repository `https://github.com/comocheng/bm_project`

Acknowledgement

The authors thank the Cantera developer team, especially Dr. Rymond Speth, Dr. Bryan Weber, and Dr. Ingmar Schoegl, as well as Chris Blais, Bjarne Kreitz, Sevy Harris, Nora Khalil, and Sun Su for helpful suggestions. This material is based upon work supported by the National Science Foundation under Grant No. #1931389. This work was also partially supported by the Exascale Catalytic Chemistry (ECC) Project, which is supported by the U.S Department of Energy, Office of Science, Basic Energy Sciences, Chemical Sciences, Geosciences and Biosciences Division, as part of the Computational Chemistry Sciences Program. The computational work was performed in part using computing resources from the Discovery cluster supported by Northeastern University's Research Computing team.

References

1. Hu, X.; Yip, A. C. K. Heterogeneous Catalysis: Enabling a Sustainable Future. *Frontiers in Catalysis* **2021**, *1*, DOI: 10.3389/fctls.2021.667675.

2. Farina, D. S.; Sirumalla, S. K.; Mazeau, E. J.; West, R. H. Extensive High-Accuracy Thermochemistry and Group Additivity Values for Halocarbon Combustion Modeling. *Industrial & Engineering Chemistry Research* **2021**, *60*, 15492–15501, DOI: 10.1021/acs.iecr.1c03076.

3. Goldsmith, C. F.; Ismail, H.; Abel, P. R.; Green, W. H. Pressure and temperature

dependence of the reaction of vinyl radical with alkenes II: Measured rates and predicted product distributions for vinyl+propene. *Proceedings of the Combustion Institute* **2009**, *32*, 139–148, DOI: 10.1016/j.proci.2008.06.142.

4. Grabow, L. C.; Mavrikakis, M. Mechanism of Methanol Synthesis on Cu through CO2 and CO Hydrogenation. *ACS Catalysis* **2011**, *1*, 365–384, DOI: 10.1021/cs200055d.

5. Kreitz, B.; Sargsyan, K.; Blöndal, K.; Mazeau, E. J.; West, R. H.; Wehinger, G. D.; Turek, T.; Goldsmith, C. F. Quantifying the Impact of Parametric Uncertainty on Automatic Mechanism Generation for CO2 Hydrogenation on Ni(111). *JACS Au* **2021**, *1*, 1656–1673, DOI: 10.1021/jacsau.1c00276.

6. Baz, A.; Dix, S. T.; Holewinski, A.; Linic, S. Microkinetic modeling in electrocatalysis: Applications, limitations, and recommendations for reliable mechanistic insights. *Journal of Catalysis* **2021**, *404*, 864–872, DOI: https://doi.org/10.1016/j.jcat.2021.08.043.

7. Motagamwala, A. H.; Dumesic, J. A. Microkinetic Modeling: A Tool for Rational Catalyst Design. *Chemical Reviews* **2021**, *121*, 1049–1076, DOI: 10.1021/acs.chemrev.0c00394.

8. de Carvalho, T. P.; Catapan, R. C.; Oliveira, A. A. M.; Vlachos, D. G. Microkinetic Modeling and Reduced Rate Expression of the Water–Gas Shift Reaction on Nickel. *Industrial & Engineering Chemistry Research* **2018**, *57*, 10269–10280, DOI: 10.1021/acs.iecr.8b01957.

9. Medford, A. J.; Lausche, A. C.; Abild-Pedersen, F.; Temel, B.; Schjødt, N. C.; Nørskov, J. K.; Studt, F. Activity and Selectivity Trends in Synthesis Gas Conversion to Higher Alcohols. *Topics in Catalysis* **2014**, *57*, 135–142, DOI: 10.1007/s11244-013-0169-0.

10. Abild-Pedersen, F.; Greeley, J.; Studt, F.; Rossmeisl, J.; Munter, T. R.; Moses, P. G.; Skúlason, E.; Bligaard, T.; Nørskov, J. K. Scaling properties of adsorption energies for hydrogen-containing molecules on transition-metal surfaces. *Physical Review Letters* **2007**, *99*, 4–7, DOI: 10.1103/PhysRevLett.99.016105.

11. Evans, M. G.; Polanyi, M. Inertia and driving force of chemical reactions. *Trans. Faraday Soc.* **1938**, *34*, 11–24, DOI: 10.1039/TF9383400011.

12. Bronsted, J. N. Acid and Basic Catalysis. *Chemical Reviews* **1928**, *5*, 231–338, DOI: 10.1021/cr60019a001.

13. Bligaard, T.; Norskov, J. K.; Dahl, S.; Matthiesen, J.; Christensen, C. H.; Sehested, J. The Bronsted-Evans-Polanyi relation and the volcano curve in heterogeneous catalysis. *Journal of Catalysis* **2004**, *224*, 206–217, DOI: 10.1016/j.jcat.2004.02.034.

14. Wang, S.; Vorotnikov, V.; Sutton, J. E.; Vlachos, D. G. Brønsted–Evans–Polanyi and Transition State Scaling Relations of Furan Derivatives on Pd(111) and Their Relation to Those of Small Molecules. *ACS Catalysis* **2014**, *4*, 604–612, DOI: 10.1021/cs400942u.

15. Cheng, J.; Hu, P.; Ellis, P.; French, S.; Kelly, G.; Lok, C. M. Bronsted-Evans-Polanyi Relation of Multistep Reactions and Volcano Curve in Heterogeneous Catalysis. *The Journal of Physical Chemistry C* **2008**, *112*, 1308–1311, DOI: 10.1021/jp711191j.

16. Blowers, P.; Masel, R. Engineering approximations for activation energies in hydrogen transfer reactions. *AIChE Journal* **2000**, *46*, 2041–2052, DOI: https://doi.org/10.1002/aic.690461015.

17. Bromly, J. H.; Barnes, F. J.; Muris, S.; You, X.; Haynes, B. S. Kinetic and Thermodynamic Sensitivity Analysis of the NO-Sensitised Oxidation of Methane. *Combustion Science and Technology* **1996**, *115*, 259–296, DOI: 10.1080/00102209608935532.

18. Vom Lehn, F.; Cai, L.; Pitsch, H. Sensitivity analysis, uncertainty quantification, and optimization for thermochemical properties in chemical kinetic combustion models. *Proceedings of the Combustion Institute* **2019**, *37*, 771–779, DOI: https://doi.org/10.1016/j.proci.2018.06.188.

19. Lausche, A. C.; Medford, A. J.; Khan, T. S.; Xu, Y.; Bligaard, T.; Abild-Pedersen, F.; Nørskov, J. K.; Studt, F. On the effect of coverage-dependent adsorbate–adsorbate interactions for CO methanation on transition metal surfaces. *Journal of Catalysis* **2013**, *307*, 275–282, DOI: https://doi.org/10.1016/j.jcat.2013.08.002.

20. Lym, J.; Gu, G. H.; Jung, Y.; Vlachos, D. G. Lattice Convolutional Neural Network Modeling of Adsorbate Coverage Effects. *The Journal of Physical Chemistry C* **2019**, *123*, 18951–18959, DOI: 10.1021/acs.jpcc.9b03370.

21. Bajpai, A.; Frey, K.; Schneider, W. F. Comparison of Coverage-Dependent Binding Energy Models for Mean-Field Microkinetic Rate Predictions. *Langmuir* **2020**, *36*, 465–474, DOI: 10.1021/acs.langmuir.9b03563.

22. Goodwin, D. G.; Speth, R. L.; Moffat, H. K.; Weber, B. W. Cantera: An Object-oriented Software Toolkit for Chemical Kinetics, Thermodynamics, and Transport Processes. https://www.cantera.org, 2021; Version 2.5.1.

23. Ashcroft, A. T.; Cheetham, A. K.; Green, M. L. H.; Vernon, P. D. F. Partial oxidation of methane to synthesis gas using carbon dioxide. *Nature* **1991**, *352*, 225–226, DOI: 10.1038/352225a0.

24. Mazeau, E. J.; Satpute, P.; Blöndal, K.; Goldsmith, C. F.; West, R. H. Automated Mechanism Generation Using Linear Scaling Relationships and Sensitivity Analyses Applied to Catalytic Partial Oxidation of Methane. *ACS Catalysis* **2021**, *11*, 7114–7125, DOI: 10.1021/acscatal.0c04100.

25. Horn, R.; Williams, K.; Degenstein, N.; Bitsch-Larsen, A.; Dalle Nogare, D.; Tupy, S.; Schmidt, L. Methane catalytic partial oxidation on autothermal Rh and Pt foam catalysts: Oxidation and reforming zones, transport effects, and approach to thermodynamic equilibrium. *Journal of Catalysis* **2007**, *249*, 380–393, DOI: 10.1016/j.jcat.2007.05.011.

26. Gao, C. W.; Allen, J. W.; Green, W. H.; West, R. H. Reaction Mechanism Generator: automatic construction of chemical kinetic mechanisms. *Computer Physics Communications* **2016**, *203*, 212–225, DOI: 10.1016/j.cpc.2016.02.013.

27. Liu, M.; Grinberg Dana, A.; Johnson, M. S.; Goldman, M. J.; Jocher, A.; Payne, A. M.; Grambow, C. A.; Han, K.; Yee, N. W.; Mazeau, E. J.; Blondal, K.; West, R. H.; Goldsmith, C. F.; Green, W. H. Reaction Mechanism Generator v3.0: Advances in Automatic Mechanism Generation. *Journal of Chemical Information and Modeling* **2021**, *61*, 2686–2696, DOI: 10.1021/acs.jcim.0c01480.

28. Blowers, P.; Masel, R. I. Extensions of the Marcus equation for the prediction of approximate transition state geometries in hydrogen transfer and methyl transfer reactions. *Theoretical Chemistry Accounts* **2000**, *105*, 46–54, DOI: 10.1007/s002140000185.

29. Blowers, P.; Masel, R. I. An ab Initio Calculation of the Potential for the Interaction of a Hydrogen Atom with an Ethane Molecule. *The Journal of Physical Chemistry A* **1999**, *103*, 7725–7729, DOI: 10.1021/jp9920951.

30. Westley, F. Table of Recommended Rate Constants for Chemical Reactions Occurring in Combustion. *NBS National Standard Reference Data Series (NSRDS)* **1980**,

31. Winther, K. T.; Hoffmann, M. J.; Boes, J. R.; Mamun, O.; Bajdich, M.; Bligaard, T. Catalysis-Hub.org, an open electronic structure database for surface reactions. *Scientific Data* **2019**, *6*, 75, DOI: 10.1038/s41597-019-0081-y.

32. Kropp, T.; Mavrikakis, M. Brønsted–Evans–Polanyi relation for CO oxidation on metal oxides following the Mars–van Krevelen mechanism. *Journal of Catalysis* **2019**, *377*, 577–581, DOI: https://doi.org/10.1016/j.jcat.2019.08.002.

33. Schumann, J.; Medford, A. J.; Yoo, J. S.; Zhao, Z.-J.; Bothra, P.; Cao, A.; Studt, F.; Abild-Pedersen, F.; Nørskov, J. K. Selectivity of Synthesis Gas Conversion to C2+ Oxygenates on fcc(111) Transition-Metal Surfaces. *ACS Catalysis* **2018**, *8*, 3447–3453, DOI: 10.1021/acscatal.8b00201.

34. Speth, R. L.; Weber, B. W.; Schoegl, I. Cantera: YAML Input File Reference. https://cantera.org/dev/yaml/, 2024; Retrieved 2024-02-23.

35. Goldsmith, C. F. Estimating the Thermochemistry of Adsorbates Based Upon Gas-Phase Properties. *Topics in Catalysis* **2012**, *55*, 366–375, DOI: 10.1007/s11244-012-9805-3.

36. Blondal, K.; Jelic, J.; Mazeau, E.; Studt, F.; West, R. H.; Goldsmith, C. F. Computer-Generated Kinetics for Coupled Heterogeneous/Homogeneous Systems: A Case Study in Catalytic Combustion of Methane on Platinum. *Industrial & Engineering Chemistry Research* **2019**, *58*, 17682–17691, DOI: 10.1021/acs.iecr.9b01464.

37. Kresse, G.; Furthmüller, J. Efficient iterative schemes for ab initio total-energy calculations using a plane-wave basis set. *Phys. Rev. B* **1996**, *54*, 11169–11186, DOI: 10.1103/PhysRevB.54.11169.

38. Kresse, G.; Furthmüller, J. Efficiency of ab-initio total energy calculations for metals and semiconductors using a plane-wave basis set. *Computational Materials Science* **1996**, *6*, 15–50, DOI: https://doi.org/10.1016/0927-0256(96)00008-0.

39. Wellendorff, J.; Lundgaard, K. T.; Møgelhøj, A.; Petzold, V.; Landis, D. D.; Nørskov, J. K.; Bligaard, T.; Jacobsen, K. W. Density functionals for surface science: Exchange-correlation model development with Bayesian error estimation. *Phys. Rev. B* **2012**, *85*, 235149, DOI: 10.1103/PhysRevB.85.235149.

40. Bahn, S.; Jacobsen, K. An object-oriented scripting interface to a legacy electronic structure code. *Computing in Science & Engineering* **2002**, *4*, 56–66, DOI: 10.1109/5992.998641.

41. Susnow, R. G.; Dean, A. M.; Green, W. H.; Peczak, P.; Broadbelt, L. J. Rate-Based Construction of Kinetic Models for Complex Systems. *The Journal of Physical Chemistry A* **1997**, *101*, 3731–3740, DOI: 10.1021/jp9637690.

42. Quiceno, R.; Pérez-Ramírez, J.; Warnatz, J.; Deutschmann, O. Modeling the high-temperature catalytic partial oxidation of methane over platinum gauze: Detailed gas-phase and surface chemistries coupled with 3D flow field simulations. *Applied Catalysis A: General* **2006**, *303*, 166–176, DOI: https://doi.org/10.1016/j.apcata.2006.01.041.

43. Mhadeshwar, A. B.; Vlachos, D. G. A Catalytic Reaction Mechanism for Methane Partial Oxidation at Short Contact Times, Reforming, and Combustion, and for Oxygenate Decomposition and Oxidation on Platinum. *Industrial & Engineering Chemistry Research* **2007**, *46*, 5310–5324, DOI: 10.1021/ie070322c.

44. Burke, M. P.; Chaos, M.; Ju, Y.; Dryer, F. L.; Klippenstein, S. J. Comprehensive H2/O2 kinetic model for high-pressure combustion. *International Journal of Chemical Kinetics* **2012**, *44*, 444–474, DOI: https://doi.org/10.1002/kin.20603.

45. Virtanen, P.; Gommers, R.; Oliphant, T. E.; Haberland, M.; Reddy, T.; Cournapeau, D.; Burovski, E.; Peterson, P.; Weckesser, W.; Bright, J.; van der Walt, S. J.; Brett, M.; Wilson, J.; Millman, K. J.; Mayorov, N.; Nelson, A. R. J.; Jones, E.; Kern, R.; Larson, E.; Carey, C. J.; Polat, İ.; Feng, Y.; Moore, E. W.; VanderPlas, J.; Laxalde, D.; Perktold, J.; Cimrman, R.; Henriksen, I.; Quintero, E. A.; Harris, C. R.; Archibald, A. M.; Ribeiro, A. H.; Pedregosa, F.; van Mulbregt, P.; SciPy 1.0 Contributors SciPy 1.0: Fun-

damental Algorithms for Scientific Computing in Python. *Nature Methods* **2020**, *17*, 261–272, DOI: 10.1038/s41592-019-0686-2.

46. Campbell, C. T. The Degree of Rate Control: A Powerful Tool for Catalysis Research. *ACS Catalysis* **2017**, *7*, 2770–2779, DOI: 10.1021/acscatal.7b00115.

TOC Graphic

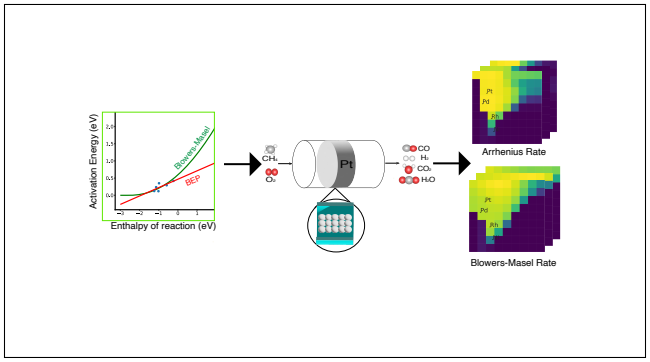
Activation Energy (eV)
Enthalpy of reaction (eV)
Blowers-Masel
BEP
CH₄
O₂
Pt
CO
H₂
CO₂
H₂O
Arrhenius Rate
Blowers-Masel Rate

Supporting Information

Implementing Blowers-Masel Approximation to Scale Activation Energy Based on Reaction Enthalpy in Mean-field Micro-kinetic Modeling for Catalytic Methane Partial Oxidation

Chao Xu[a], Emily Mazeau[a,b], Richard H. West[a]

[a] *Department of Chemical Engineering, Northeastern University, Boston, MA, USA*
[b] *Oak Ridge National Laboratory, Oak Ridge, TN 37830, USA*

Email address: r.west@northeastern.edu (Richard H. West)

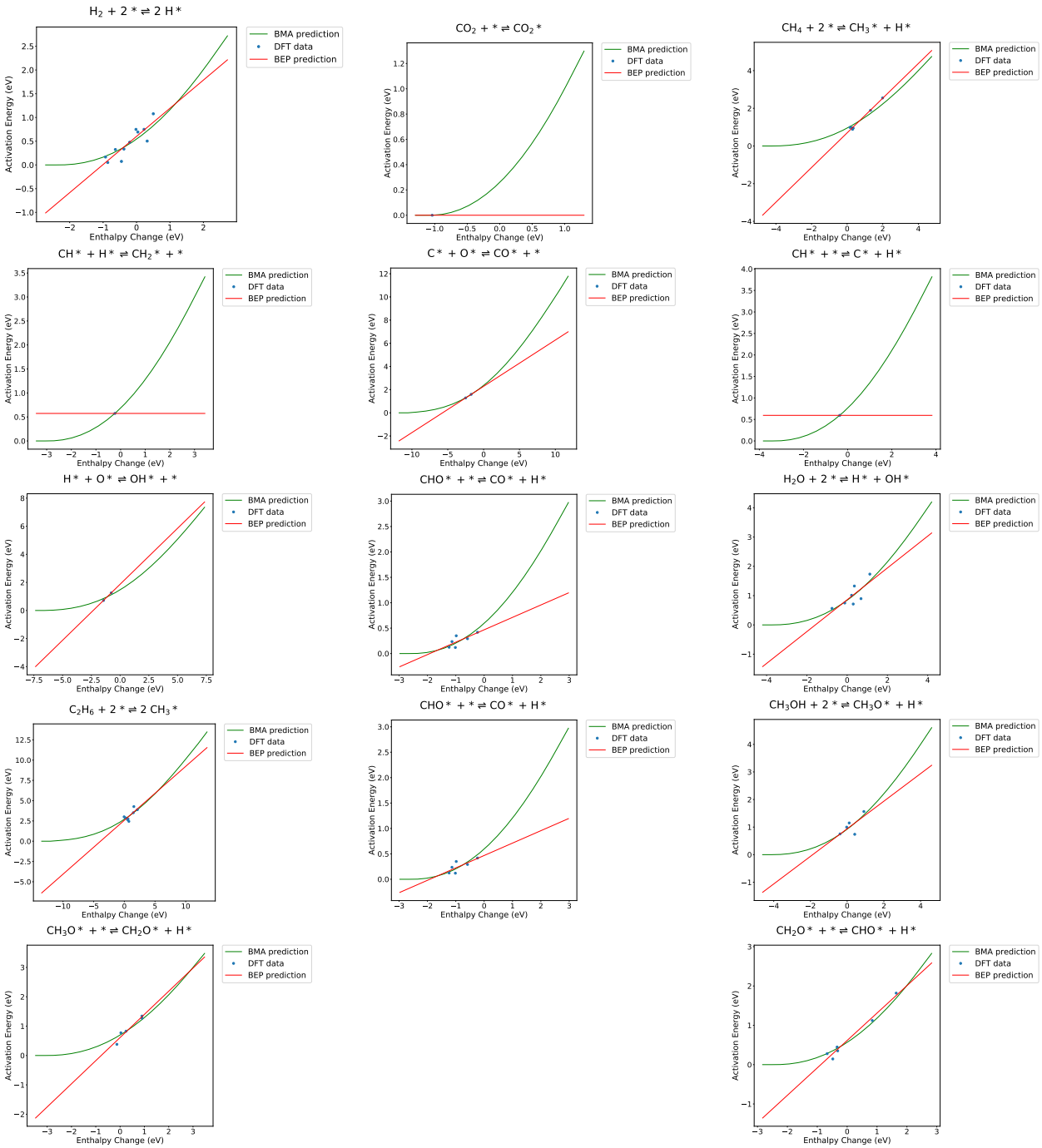

Figure S1: BMA fittings for the data extracted from Catalysis-Hub

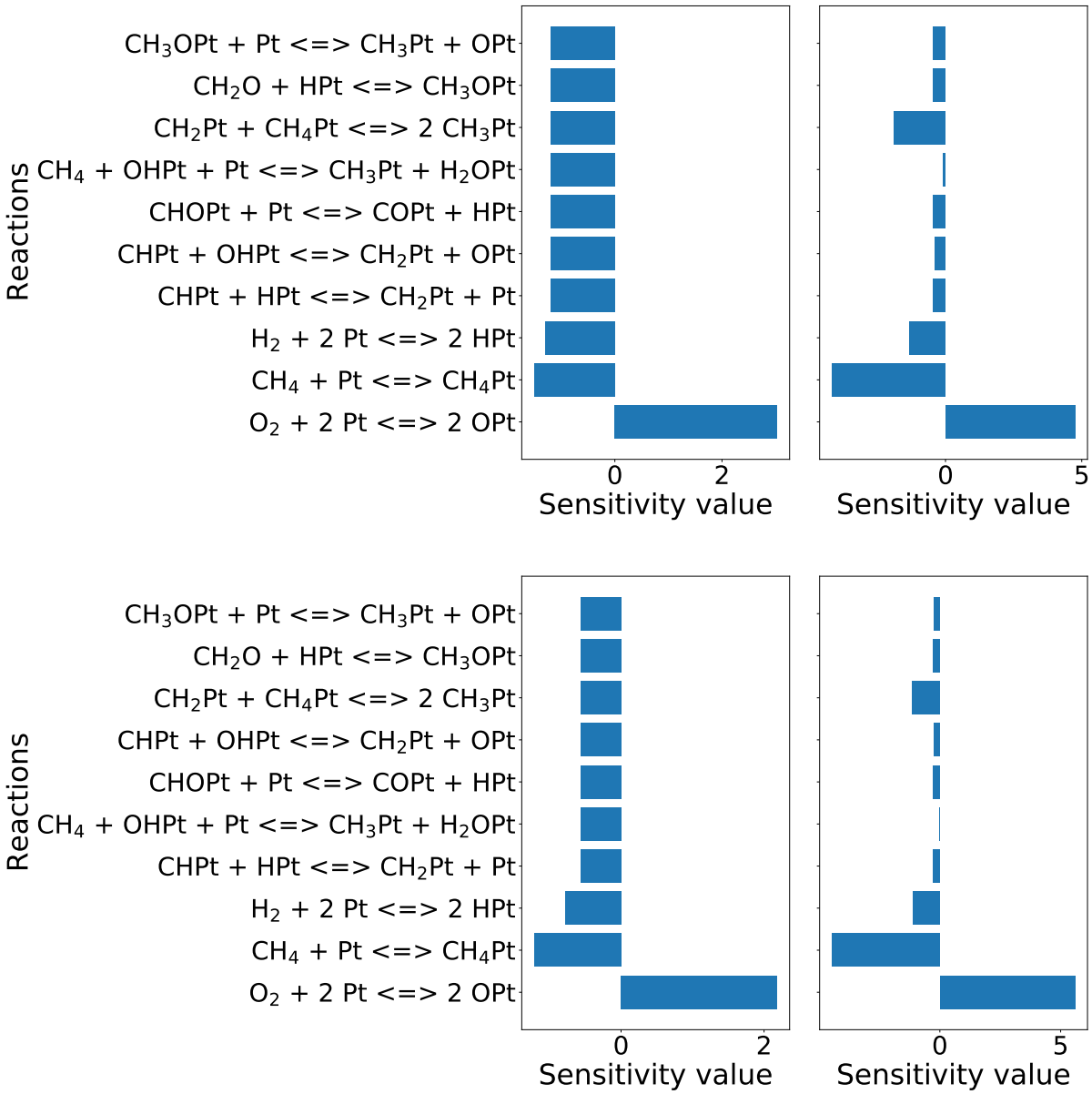

Figure S2: Kinetic sensitivity of synthesis gas yield (top plot) and full oxidation (bottom plot) comparison for the CMPO (left) and CMPO-BMA (right) base Pt(111) models at C/O=1.0

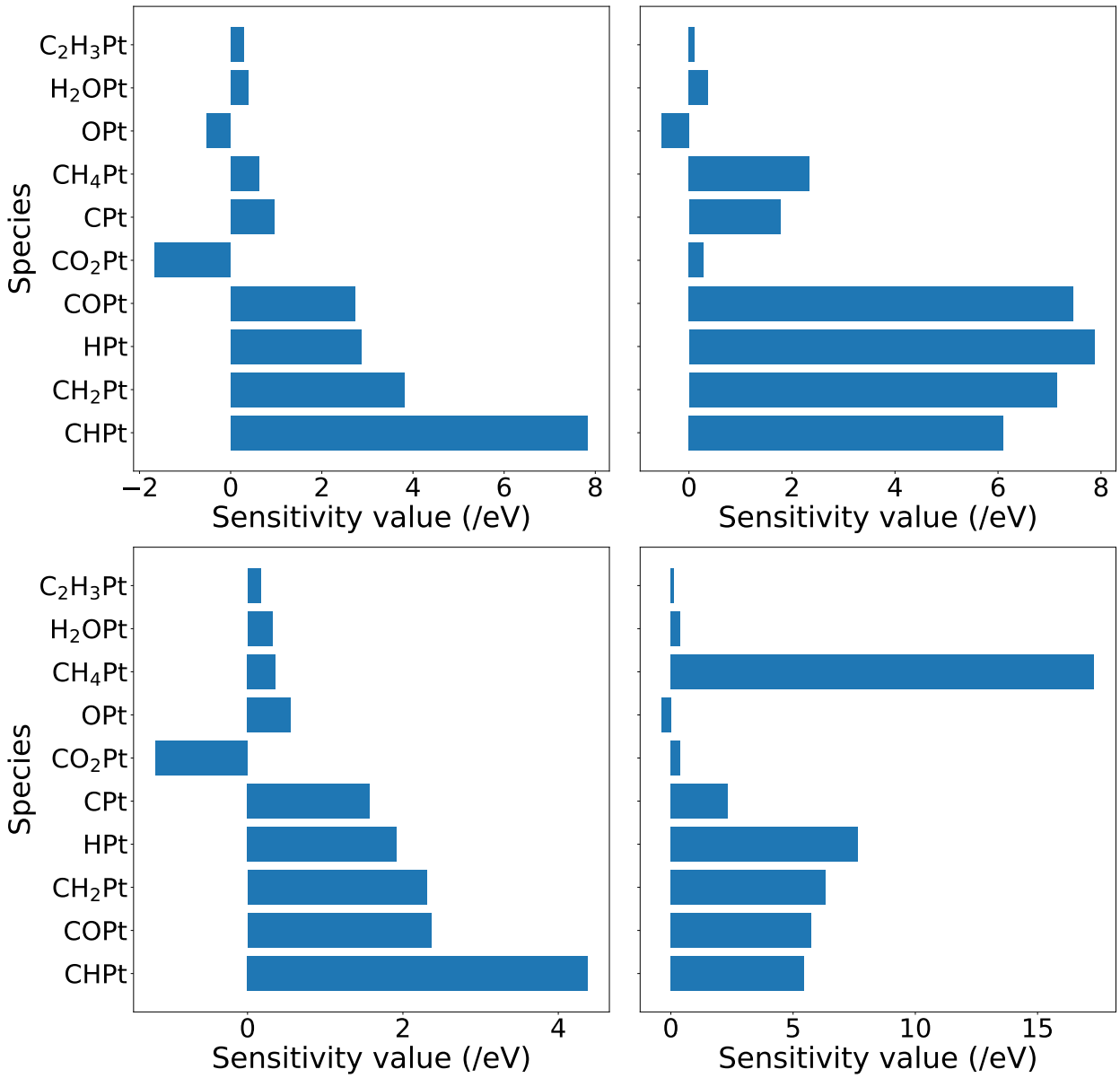

Figure S3: Thermodynamic sensitivity of sythesis gas conversion (top plot) and full oxidation (bottom plot) comparison for the CMPO (left) and CMPO-BMA (right) base Pt(111) models at C/O=1.0

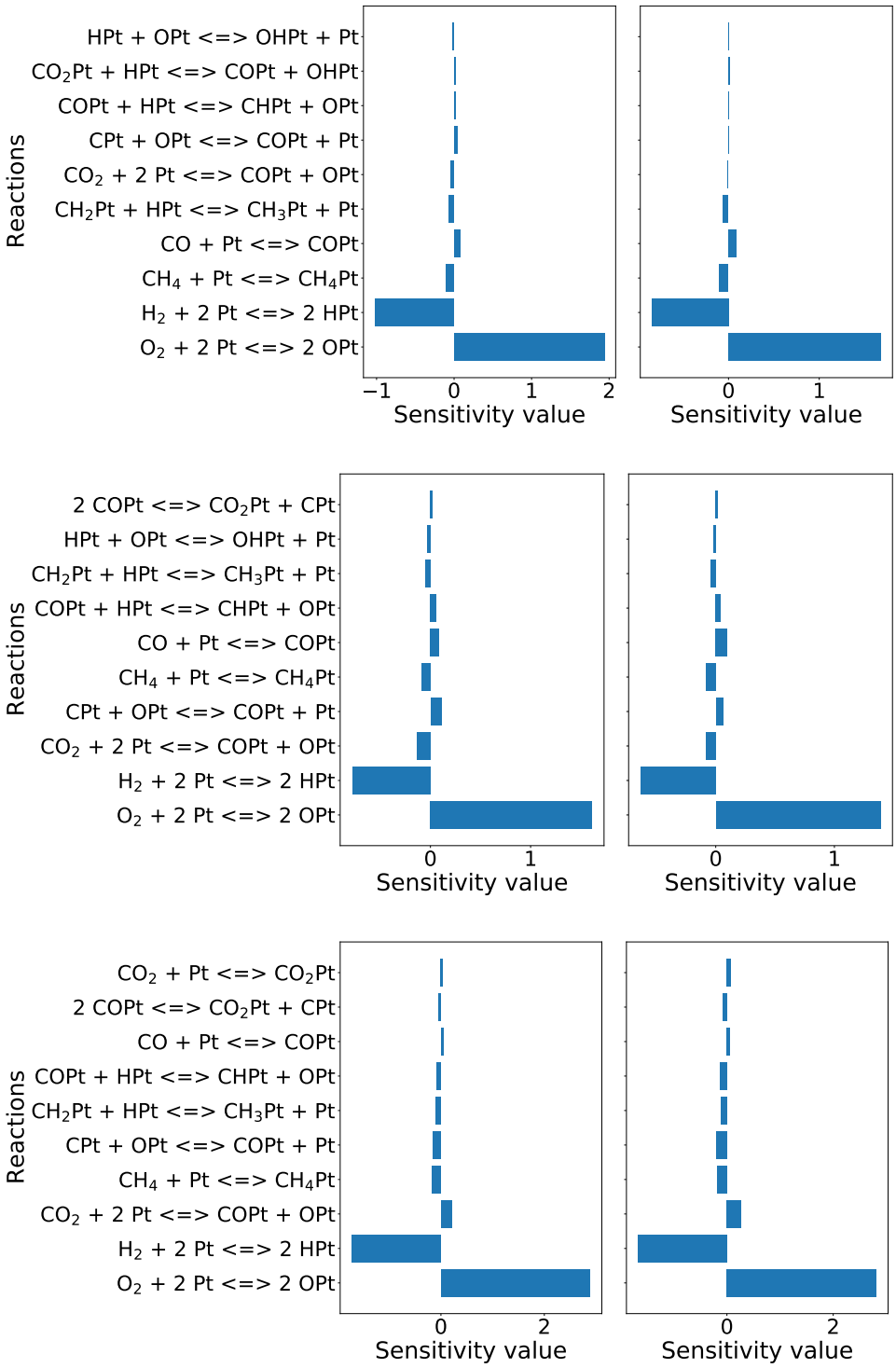

Figure S4: Kinetic sensitivity of CH_4 conversion (top plot), synthesis gas yield (middle plot), and full oxidation (bottom plot) comparisons for the CMPO (left) and CMPO-BMA (right) base Pt(111) models at C/O=2.6

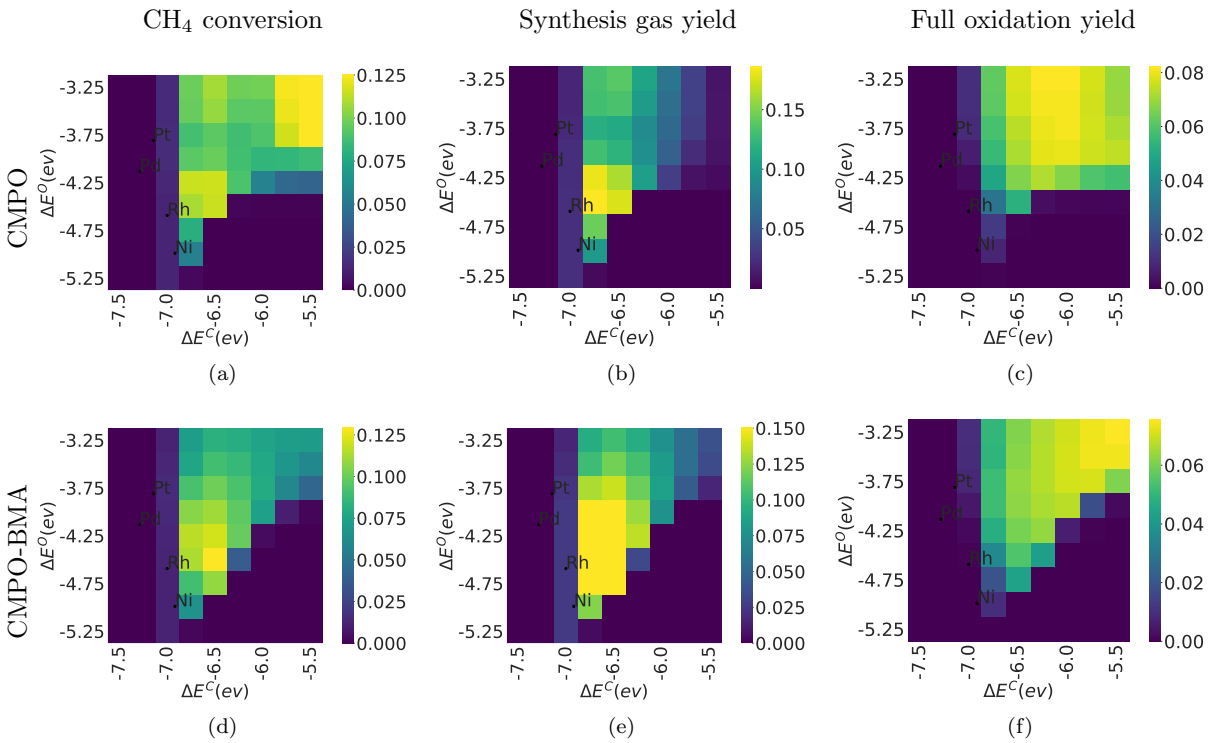

Figure S5: Comparison of CH_4 conversion, synthesis gas yield, and full oxidation yield at C/O=2.6 between CMPO ((a),(b),(c)) and CMPO-BMA ((d),(e),(f)) models. The y-axis represents the binding energy of atomic oxygen, and the x-axis represents the binding energy of atomic carbon, each pixel represents a hypothetical metal interface

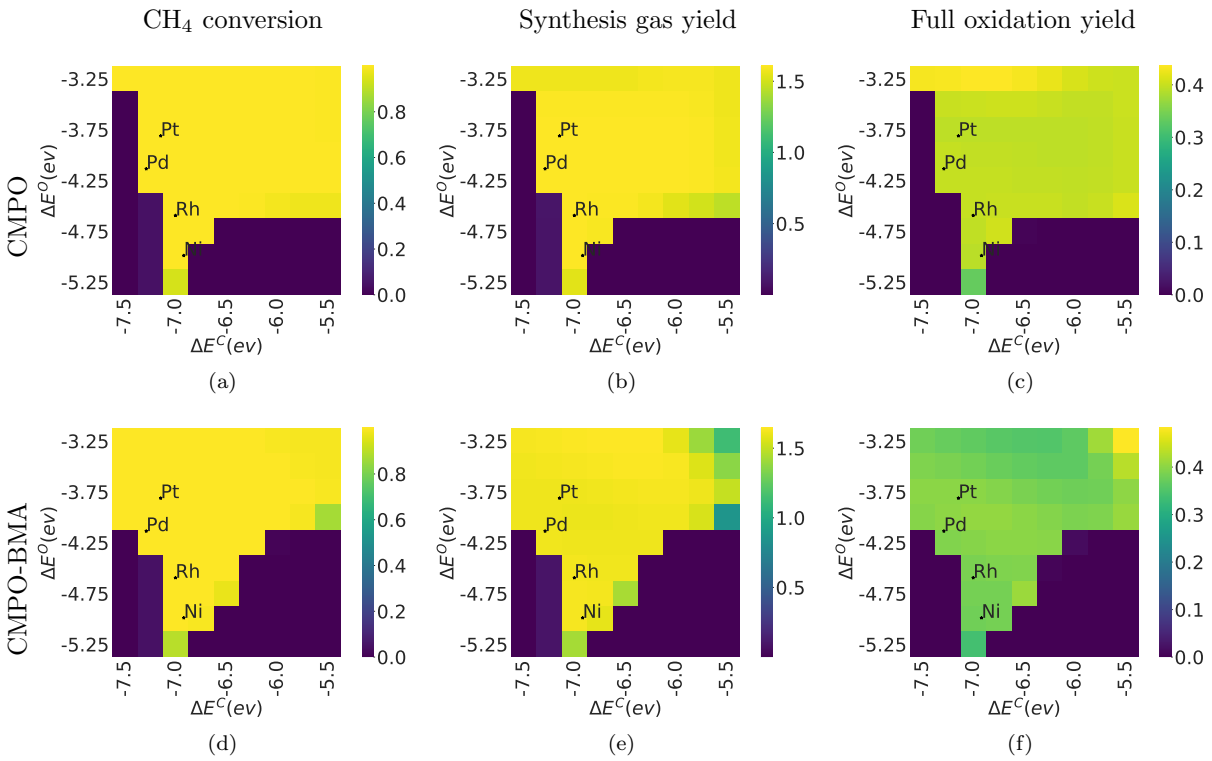

Figure S6: Comparison of CH_4 conversion, synthesis gas yield, and full oxidation yield at C/O=0.6 at the end of PFR between CMPO ((a),(b),(c)) and CMPO-BMA ((d),(e),(f)) models over 81 hypothetical metals. The y-axis represents the binding energy of atomic oxygen, and the x-axis represents the binding energy of atomic carbon, each pixel represents a hypothetical metal interface.

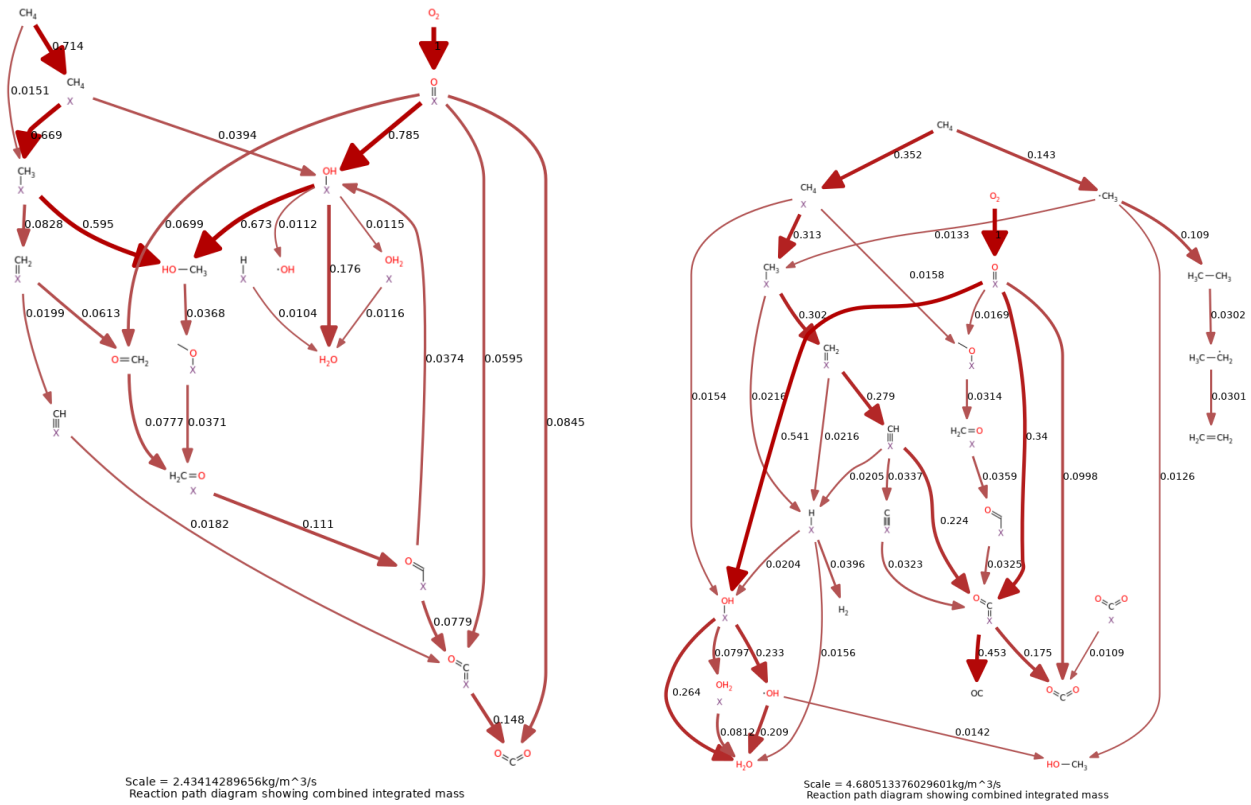

(a) Reaction path for CMPO model

(b) Reaction path for CMPO-BMA model

Figure S7: Comparison of the reaction paths in the CMPO and CMPO-BMA models on metal at ($\Delta E^O = -3.25$ eV, $\Delta E^C = -6.0$ eV). Line widths and labels indicate the net mass flux integrated from 0 to 1.045 cm in the reactor. The CMPO model makes lots of gas-phase methanol CH_3OH from the adsorbed CH_3*, whereas on the CMPO-BMA model adsorbed CH_3* continues to react via CH_2* and CH* to eventually make CO and CO_2.

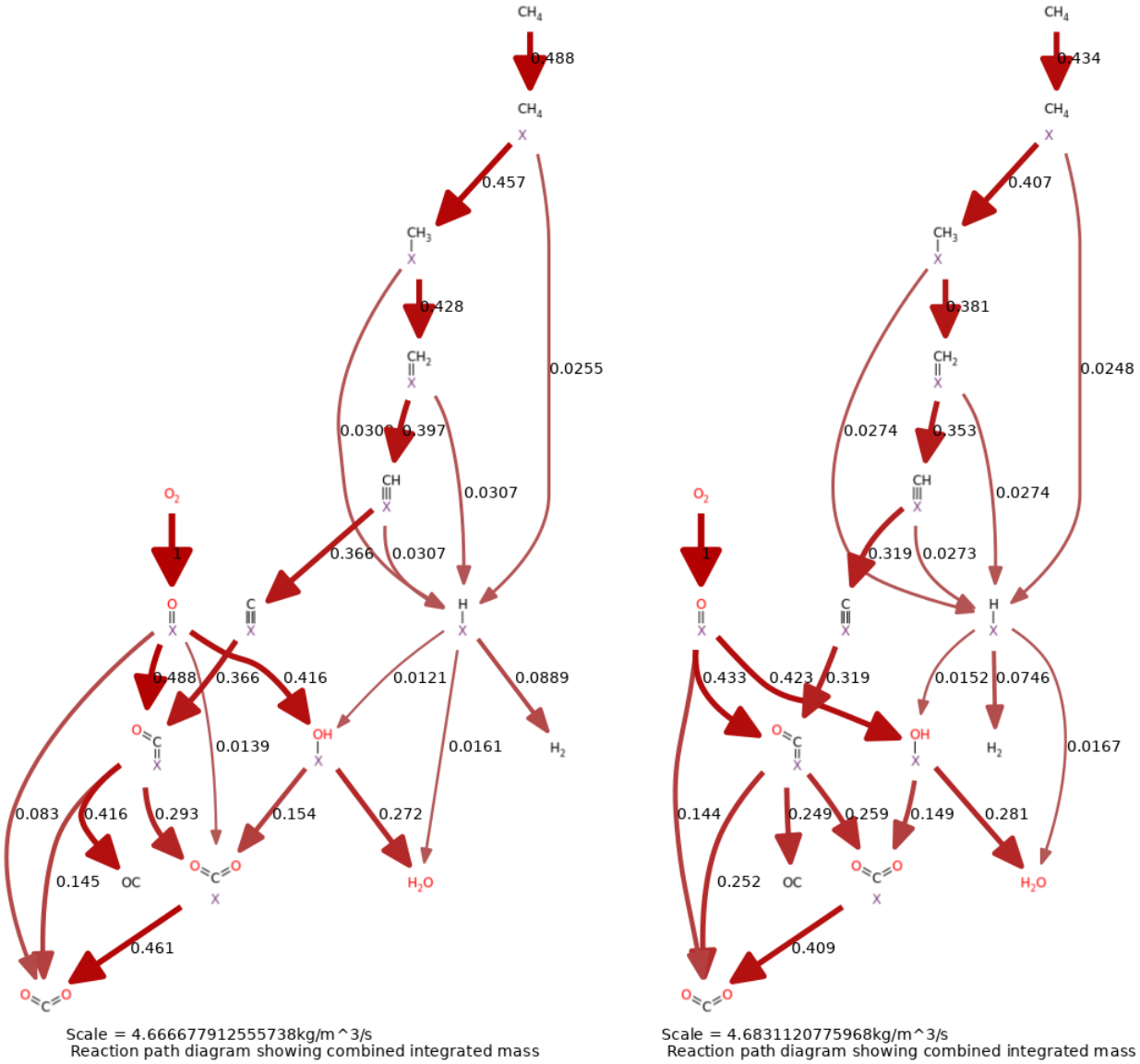

(a) Reaction path for CMPO model

(b) Reaction path for CMPO-BMA model

Figure S8: Comparison of the reaction paths in the CMPO and CMPO-BMA models on metal at ($\Delta E^O = -4.25$ eV, $\Delta E^C = -7.25$ eV). Line widths and labels indicate the net mass flux integrated from 0 to 1.045 cm in the reactor. They are quite similar.